JCTC Journal of Chemical Theory and Computation

Article

pubs.acs.org/JCTC

Free Energy Surface Reconstruction from Umbrella Samples Using Gaussian Process Regression

Thomas Stecher,*[,†] Noam Bernstein,[‡] and Gábor Csányi*[,†]

[†]Department of Engineering, University of Cambridge, Trumpington Street, Cambridge, CB2 1PZ, U.K.

[‡]Naval Research Laboratory, Center for Computational Materials Science, Washington, D.C. 20375, United States

ABSTRACT: We demonstrate how the Gaussian process regression approach can be used to efficiently reconstruct free energy surfaces from umbrella sampling simulations. By making a prior assumption of smoothness and taking account of the sampling noise in a consistent fashion, we achieve a significant improvement in accuracy over the state of the art in two or more dimensions or, equivalently, a significant cost reduction to obtain the free energy surface within a prescribed tolerance in both regimes of spatially sparse data and short sampling trajectories. Stemming from its Bayesian interpretation the method provides meaningful error bars without significant additional computation. A software implementation is made available on www.libatoms.org.

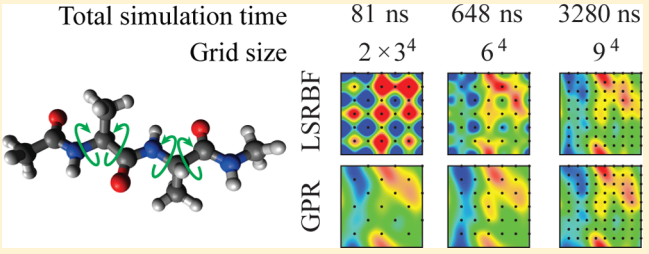

1. INTRODUCTION

Free energy is a central quantity in materials science and physical chemistry, governing the macroscopic behavior of a system in the presence of thermal fluctuations. It is defined as a function of a limited number of collective variables and includes the effects of energy as well as entropy, averaged over thermal fluctuations in the remaining degrees of freedom. The progress of any microscopic process occurring in or near equilibrium, including reactions and phase transformations, is controlled by the free energy surface in the space of appropriately chosen collective variables. Many methods exist for computing free energies or their differences, based on various aspects and properties of the free energy.

Formally, the free energy is the logarithm of the marginal probability density of the system in equilibrium corresponding to the chosen thermodynamic ensemble. A crude and naïve approach would therefore be to estimate the probability density (e.g., by constructing histograms) from samples obtained in a direct molecular dynamics (MD) or Monte Carlo (MC) simulation. This is almost never practical in scientifically interesting cases due to the presence of large barriers and metastable states which cannot be representatively sampled directly on the time scale of a typical direct simulation. One solution to this problem is to restrain the sampling to specific areas of interest by altering the Hamiltonian through an additional potential term, often called a *bias*. This is the umbrella or non-Boltzmann sampling approach and goes back to Torrie and Valleau,[1] who showed how to recover the unbiased probability distribution from the biased one.

In this paper we focus on the question of how to efficiently use the data coming from a set of such biased simulations. Traditional methods include the Weighted Histogram Analysis Method (WHAM)[2,3] and the Umbrella Integration (UI)[4,5] technique, including its multidimensional variant[6,7] which uses least-squares fitting of radial basis functions (LSRBF)[8] to reconstruct the free energy surface. The former takes direct advantage of the relation between the free energy and the marginal probability distribution of a system; the latter—like thermodynamic integration[9] on which it is based—reconstructs the free energy from the mean (i.e., thermodynamically averaged) force in each biased simulation, which under suitable conditions is the negative gradient of the free energy. Recently a number of maximum-likelihood approaches operating on the probability distribution, such as multistate Bennett acceptance ratio (MBAR),[10] which has been shown to be equivalent to a binless WHAM,[11] and variational free energy profile (vFEP),[12,13] have been proposed that go some way to eliminate the shortcomings of WHAM.

Working with more than one collective coordinate significantly adds to the challenge of free energy surface reconstruction. The most obvious problem, which gets exponentially harder as the number of dimensions increases, is exploration, i.e. the problem of ensuring that the entire region of interest is sufficiently sampled. The principal difficulty is a chicken-and-egg problem: before the free energy surface is reconstructed, it is not possible to know which regions of collective variable space correspond to low free energies and therefore are relevant.

Some approaches, such as metadynamics[14] and the adaptive biasing force (ABF) method,[15,16] combine exploration and reconstruction by gradually building up an approximate bias potential that is designed to converge to the negative of the free energy and thus counteract the natural occupancy bias of the

Received: May 21, 2014

   dx.doi.org/10.1021/ct500438v | *J. Chem. Theory Comput.* XXXX, XXX, XXX−XXX

Boltzmann distribution toward low free energy regions. Metadynamics does this based on where the system has been, i.e. its observed probability density, while ABF uses sampled free energy gradients. Another approach is to separate exploration from reconstruction, as in the "single-sweep" method.[6] In this approach, temperature-accelerated molecular dynamics[17]—an extension of adiabatic free energy dynamics[18,19]—is used in a first step to identify a small number of points in the "important regions of the free energy landscape".[6] At these points free energy gradients are calculated using independent standard umbrella sampling simulations and then, in the second step, the free energy surface is reconstructed from these gradients using LSRBF. Recently, Tuckerman and coworkers[20] proposed what amounts to a synthesis of metadynamics and the single-sweep method, combining dynamics at a higher temperature in the (adiabatically decoupled) collective variables with an on-the-fly construction of a bias potential to steer the system away from regions in collective-variable space already visited. The free energy is again reconstructed from measurements of its gradients in umbrella simulations and least-squares fitting (but using fewer basis functions compared to the original "single sweep" method).

Gaussian mixtures umbrella sampling (GAMUS) is another recently published combined exploration-reconstruction method, in which the probability distribution is modeled by a sum of Gaussians whose parameters are determined using the Expectation-Maximization algorithm.[21] The authors warn that it is primarily useful for exploration and not for determining the free energy profile accurately.

In the present work, we do not tackle the first task of exploration; rather, we seek to showcase the Gaussian process regression (GPR) framework for performing the second task of free energy reconstruction from independent umbrella simulations. In the one-dimensional case only, exploration rarely preoccupies the modeler: usually a simple uniform grid over the range of interest suffices. In more than one dimension we wish to demonstrate how GPR compares with LSRBF and vFEP. LSRBF is known to have problems with large condition numbers in cases where the data density is high,[6,8] and both it and vFEP will be shown below to be rather intolerant of noise in the data. Because the simulations needed for exploration and collection of free energy gradients are so computationally expensive, the post hoc reconstruction of the free energy surface is a negligible part of the overall computational cost for all the methods we investigate and therefore we omit discussion of computational cost directly associated with the free energy surface reconstruction.

Bayesian statistics is a natural framework for function fitting, allowing us not only to express our prior beliefs about the smoothness of the free energy function in terms of a prior probability distribution defined on a Hilbert space of a large class of possible functions, but also to treat consistently the often significant sampling noise arising from the limited time span of the trajectories. More specifically, GPR is an ideal technique for our purposes, because the evaluation of the reconstructed free energy function is analytically tractable, and one does not have to perform further sampling just to evaluate the reconstructed function, as is often the case with more complex Bayesian techniques. The GPR framework allows one to incorporate all the useful data from the MD trajectories in a consistent fashion, including both histograms and measurements of free energy derivatives. Our exposition of the theory behind the GPR is nevertheless rather basic, because there are excellent text books on the subject. Our purpose is to illustrate the kinds of benefits these types of methods can offer for free energy reconstruction, and more sophisticated reconstruction algorithms are possible based on the available statistics and machine learning literature.

Indeed the use of Gaussian processes for prediction and interpolation problems is widespread. While the basic theory came from time series analysis,[22,23] it became popular in the field of geostatistics under the name "kriging".[24] O'Hagan[25] generalized the theory, while Williams and Rasmussen[26,27] brought the approach to machine learning, thus disseminating it to a wider community. In the field of physical chemistry, Bartók et al. recently used it to create highly accurate potential energy surfaces for selected materials by interpolating ab initio energies and forces,[28,29] while Rupp et al. interpolated the atomization energies of a wide range of molecules,[30] and Handley et al. interpolated electrostatic multipoles.[31]

The paper is structured as follows: In section 2 we briefly review umbrella sampling and the WHAM and UI techniques for free energy reconstruction to define our notation, and then describe the formalism of Gaussian process regression. In section 3 we propose a free energy reconstruction method that combines umbrella sampling, histogram analysis and GPR. In section 4 we introduce an alternative method which uses GPR to reconstruct a free energy profile from the mean forces obtained from the same data, before showing in section 4.2 how in fact the two strategies can be combined in a consistent manner. We discuss error estimates in section 5. We compare the numerical performance of our approaches to that of WHAM, UI, LSRBF and vFEP in section 6.

2. BACKGROUND THEORY

2.1. Umbrella Sampling. Umbrella sampling[1] provides the means to obtain and use samples from biased MD or MC simulations in free energy reconstructions and related problems. Biased sampling is necessary whenever the system of interest has appreciable energetic or entropic barriers. In such cases the transitions between metastable states separated by these barriers occur over a much longer time scale than that of the fast molecular vibrations that put a strong lower bound on the time resolution of the simulation, and a corresponding constraint on the total simulation time possible given fixed computational resources. It would therefore not be possible to obtain an accurate representation of the global probability distribution in configuration space without biasing.

In the following we write $\beta = 1/k_B T$ for the inverse temperature, $\mathbf{q}$ for the configurational degrees of freedom of the system, $x = s(\mathbf{q})$ for the collective variable of interest, $V(\mathbf{q})$ for the potential energy, and

$$Z = \int e^{-\beta V(\mathbf{q})}\, \mathrm{d}\mathbf{q} \tag{1}$$

for the configurational partition function of the system. Biasing is achieved by the addition of a restraining potential $w(s(\mathbf{q}))$, often chosen to be harmonic. This changes the original, unbiased probability density of the system

$$P(x) = \frac{1}{Z} \int e^{-\beta V(\mathbf{q})} \delta(s(\mathbf{q}) - x)\, \mathrm{d}\mathbf{q} \tag{2}$$

to the biased distribution

dx.doi.org/10.1021/ct500438v | J. Chem. Theory Comput. XXXX, XXX, XXX−XXX

$$P^{\mathrm{b}}(x) = \frac{1}{Z^{\mathrm{b}}}\int e^{-\beta[V(\mathbf{q})+w(s(\mathbf{q}))]}\delta(s(\mathbf{q}) - x)\,\mathrm{d}\mathbf{q} = \frac{1}{Z^{\mathrm{b}}}e^{-\beta w(x)}\int e^{-\beta V(\mathbf{q})}\delta(s(\mathbf{q}) - x)\,\mathrm{d}\mathbf{q} \tag{3}$$

where

$$Z^{\mathrm{b}} = \int e^{-\beta[V(\mathbf{q})+w(s(\mathbf{q}))]}\,\mathrm{d}\mathbf{q} \tag{4}$$

is the configurational partition function of the biased system. The unbiased distribution can thus be reconstructed from the biased distribution as[1]

$$P(x) = \frac{Z^{\mathrm{b}}}{Z}e^{\beta w(x)}P^{\mathrm{b}}(x) \tag{5}$$

However, the partition function ratio, given by the following expressions, cannot be evaluated directly because contributions from poorly sampled areas dominate the average.

$$\frac{Z^{\mathrm{b}}}{Z} = \frac{\int e^{-\beta[V(\mathbf{q})+w(s(\mathbf{q}))]}\,\mathrm{d}\mathbf{q}}{\int e^{-\beta V(\mathbf{q})}\,\mathrm{d}\mathbf{q}} = \langle e^{-\beta w(s(\mathbf{q}))}\rangle \tag{6}$$

$$= \frac{\int e^{-\beta[V(\mathbf{q})+w(s(\mathbf{q}))]}\,\mathrm{d}\mathbf{q}}{\int e^{-\beta[V(\mathbf{q})+w(s(\mathbf{q}))]}e^{+\beta w(s(\mathbf{q}))}\,\mathrm{d}\mathbf{q}} = \frac{1}{\langle e^{\beta w(s(\mathbf{q}))}\rangle_{\mathrm{b}}} \tag{7}$$

where $\langle\cdots\rangle$ denotes a canonical average of the unbiased and $\langle\cdots\rangle_{\mathrm{b}}$ a canonical average of the biased system. Equation 6 will suffer from the usual problems of unbiased sampling, i.e. convergence will only be achieved on an appreciable time-scale if the minima of V and w are close to each other, a prerequisite which defies the point of biasing. Equation 7 on the other hand will record the most significant contributions to the average where the bias potential is large and therefore the density of the biased distribution is low.

2.2. WHAM. When using methods that employ only one global (perhaps complicated) bias potential, such as metadynamics[14] or the adaptive biasing force (ABF) method,[15] the unknown normalization constant Z^{b}/Z is not needed: the unbiased probability distribution is simply reconstructed up to a multiplicative constant and, if required, renormalized *a posteriori* so that it integrates to unity. However, if samples come from several simulations, each with its own bias, as is the usual case in umbrella sampling with many umbrella windows, the unknown normalization constant will differ from window to window. WHAM[2,3] solves this problem using an iterative procedure, effectively matching the free energy, $F(x) = -1/\beta \ln P(x)$, in the overlap regions between each pair of windows. This necessitates a simulation setup which ensures good sampling of these overlap regions.

More specifically, WHAM constructs a global histogram with a set of bins spanning all umbrella simulations. Using N_θ for the total number of samples collected in window θ, the expected number of bin counts, $\langle n_{\theta i}\rangle$, in the ith bin in the biased simulation corresponding to window θ can be written in terms of the unknown unbiased bin probabilities P_i as

$$\langle n_{\theta i}\rangle = N_\theta\frac{P_i c_{\theta i}}{\sum_i P_i c_{\theta i}} \tag{8}$$

where $c_{\theta i}$ represents the multiplicative bias value in window θ against bin i, approximated by the value of the bias at the center, x_i, of each bin, i.e.

$$c_{\theta i} = e^{-\beta w_\theta(x_i)} \tag{9}$$

The sum in the denominator in eq 8 is an approximation to the biased partition function associated with the biased simulation, corresponding to window θ

$$Z_\theta^{\mathrm{b}} = \sum_i c_{\theta i}P_i$$

In order to determine the unknown unbiased probabilities P_i, eq 8 is first summed over the windows

$$\sum_\theta \langle n_{\theta i}\rangle = \sum_\theta N_\theta P_i c_{\theta i}[Z_\theta^{\mathrm{b}}]^{-1}$$

and then rearranged to express P_i,

$$P_i = \frac{\sum_\theta \langle n_{\theta i}\rangle}{\sum_\theta N_\theta[Z_\theta^{\mathrm{b}}]^{-1}c_{\theta i}} \tag{10}$$

In order to use it to recover unbiased bin probabilities from observed bin counts, we replace the expectation in the numerator by the sum of actual observed bin counts, $M_i = \Sigma_\theta n_{\theta i}$, and then solve for the set of P_is iteratively until self-consistency is achieved. It has been shown[32,33] that the solution thus obtained is equivalent to maximizing the likelihood of jointly observing the bin counts $\{M_i\}$ given underlying bin probabilities $\{P_i\}$. Indeed, Zhu and Hummer[34] have shown that maximizing the likelihood directly leads to a more efficient algorithm compared to the traditional iterative procedure.

Equation 8 can be used to directly illuminate why the distributions in the neighboring umbrella windows must overlap significantly in order for WHAM to work. With the anticipation of taking logarithms in the next step, we define $y_{\theta i}$ and $\tilde{y}_{\theta i}$ by writing the bin count values as

$$\frac{n_{\theta i}}{N_\theta} = e^{-\beta y_{\theta i}} \tag{11}$$

$$\frac{\langle n_{\theta i}\rangle}{N_\theta} = e^{-\beta \tilde{y}_{\theta i}} \tag{12}$$

so that $y_{\theta i}$ corresponds to the actually observed values and $\tilde{y}_{\theta i}$ corresponds to expectations. If we denote the unknown unbiased free energy at bin i by $F_i = -(\ln P_i)/\beta$ and the logarithm of the unknown bin partition function by $f_\theta^{\mathrm{b}} = \ln Z_\theta^{\mathrm{b}}$, then the logarithm of eq 8 becomes a set of equations, one for each i and θ,

$$F_i = \tilde{y}_{\theta i} - w_\theta(x_i) + f_\theta^{\mathrm{b}} \approx y_{\theta i} - w_\theta(x_i) + f_\theta^{\mathrm{b}} \tag{13}$$

where the value of each F_i has to be consistent for all θ, and the approximation results from replacing the expectation $\tilde{y}_{\theta i}$ by the observed $y_{\theta i}$. In addition to this approximation, if $n_{\theta i}$ happens to be zero for some particular umbrella θ and bin i, its logarithm $y_{\theta i}$ would be undefined, and the instance of eq 13 corresponding to that θ and i combination is therefore ignored. The coupling between different umbrellas occurs when a given bin has nonzero contributions from at least two umbrellas, and so all instances of eq 13 with the same i and different θ must hold with the same value of F_i. The task of finding a consistent set of values for all F_i and f_θ^{b} is equivalent to the self-consistency iteration in the conventional formulation of WHAM. However, if there exists an umbrella that has nonzero bin counts $n_{\theta i}$ only for bins that do not have any counts from any other umbrellas, there is no need for consistency, and that set of bins is

dx.doi.org/10.1021/ct500438v | J. Chem. Theory Comput. XXXX, XXX, XXX−XXX

decoupled from the rest. The free energy of that set of bins is therefore ill defined: an arbitrary constant can be added to their F_i and f_θ^b without disturbing any F_i or f_θ^b for any other bins or umbrellas, thus defeating the whole purpose of generating a globally valid reconstruction.

2.3. Umbrella Integration. An alternative approach, umbrella integration, is based on measuring the gradient of the free energy obtained from a set of simulations using strictly harmonic bias potentials

$$w_\theta(x) = \frac{1}{2}\kappa_\theta(x - x_\theta)^2 \tag{14}$$

where κ_θ is the strength of the bias potential and x_θ the window center. In each window, there is a collective variable value where the restraining force from the bias potential is exactly balanced by the free energy derivative, thus creating a stationary point in the biased distribution, namely its mode, $\hat{x}_\theta$.[4] Therefore, at the collective variable value corresponding to the mode, the free energy gradient is equal to minus the restraint gradient. In practice, however, the mode of the biased distribution is approximated by its mean, $\overline{x}_\theta$, a quantity which can be estimated much more accurately from a limited amount of data than the mode, giving the following estimated free energy gradients[4]

$$\begin{aligned} \left.\frac{\partial F(x)}{\partial x}\right|_{\hat{x}_\theta} &= -\left.\frac{\partial w_\theta}{\partial x}\right|_{\hat{x}_\theta} \\ &\downarrow\ \hat{x}_\theta \approx \overline{x}_\theta \\ \left.\frac{\partial F(x)}{\partial x}\right|_{\overline{x}_\theta} &\approx -\left.\frac{\partial w_\theta}{\partial x}\right|_{\overline{x}_\theta} = -\kappa_\theta(\overline{x}_\theta - x_\theta) \end{aligned} \tag{15}$$

The mode exactly equals the mean if the biased distribution is unimodal and symmetric,[4] and the approximation will be good if the harmonic restraining potential is sufficiently stiff. However, the variance of the estimator in ref 15 scales like $O(\kappa)$, so stronger biases lead to more statistical noise. Also, using very stiff bias potentials necessitate the use of short time-steps in the simulation and might introduce high barriers in the space perpendicular to the collective variable, thus making the sampling very inefficient.

Working with free energy derivatives rather than absolute free energies allows UI to avoid the problem of the unknown offsets or equivalent normalization constants that WHAM encounters. In one dimension it is simple to integrate the estimated gradients numerically to obtain the free energy profile. In more than one dimension one needs to ensure that the free energy surface is independent of the path of integration. One solution to this problem is provided by least-squares fitting, which we discuss in Sec. 4.1.

2.4. Gaussian Process Regression. In this section we outline the most important aspects of GPR, the main computational technique underlying our proposed method, and define notation. An in-depth introduction to GPR can be found in the textbooks.[27,35] In the most basic case, we have a number of noisy scalar readings, collected into a vector $\mathbf{y} = \{y_i\}$, of an unknown function f, at a certain number of locations $\mathbf{x} = \{x_i\}$, and we wish to predict the function value, $f(x^*)$, at a new location x^*. GPR is a Bayesian method: it combines a prior probability distribution on the function values with the data through the likelihood of measuring the observed data given the function. Formally

$$\begin{aligned} p(f(x^*)|\mathbf{y}) &= p(f(x^*) \text{ and } \mathbf{y})/p(\mathbf{y}) \\ &\propto \int \mathrm{d}\mathbf{f}(\mathbf{x}) p(f(x^*) \text{ and } \mathbf{f}(\mathbf{x})) p(\mathbf{y}|\mathbf{f}(\mathbf{x})) \end{aligned}$$

where the elements of the vector $\mathbf{f}(\mathbf{x})$ are the (unknown) values of the underlying function f at the measurement locations $\mathbf{x}$. Note that the normalizing constant of the posterior probability distribution $p(\mathbf{y})$ is typically not calculated explicitly and has been omitted on the second line. The first term of the product in the integral corresponds to the prior distribution on f and, thus, does not depend on the values of the observed data, only on its locations, while the second term is the likelihood which encodes information about the noise inherent in our measurement. The output of the GPR is the posterior distribution on the left-hand side, corresponding to the prediction at an arbitrary new location x^*. We will interpret the maximum of the posterior distribution as corresponding to the most likely reconstructed function value given the data and the prior.

In GPR the prior distribution is a Gaussian process, which describes a distribution over functions and can loosely be thought of as an infinite-dimensional multivariate Gaussian distribution or, more formally, a collection of random variables, any finite number of which have a joint Gaussian distribution.[27] Just as a multivariate Gaussian distribution is defined by a mean vector and covariance matrix, a Gaussian process is defined by a mean function $m(x)$ and a covariance function (or kernel) $k(x, x')$. Throughout this paper we will take the prior mean function to be zero, so the prior is

$$p(\mathbf{f}(\mathbf{x})) = (2\pi)^{-n/2}|K(\mathbf{x})|^{-1/2}\exp\left[-\frac{1}{2}\mathbf{f}^{\mathrm{T}}K(\mathbf{x})\mathbf{f}\right] \tag{16}$$

where n is the number of data points, $K(\mathbf{x})$ is the covariance matrix, and $|K(\mathbf{x})|$ is its determinant. The entries $K_{ij} = k(x_i, x_j)$ give the covariance between the values of the function evaluated at x_i and at x_j. We discuss the specification of the prior covariance function in more detail in the next section but, loosely, the value of the covariance between two locations indicates how close the corresponding function values are expected to be.

The measurement noise is also assumed to be joint Gaussian, i.e. the likelihood takes the form

$$p(\mathbf{y}|\mathbf{f}(\mathbf{x})) = (2\pi)^{-n/2}\left|\Sigma_y\right|^{-1/2}\exp\left[-\frac{1}{2}(\mathbf{y} - \mathbf{f}(\mathbf{x}))^{\mathrm{T}}\Sigma_y^{-1}(\mathbf{y} - \mathbf{f}(\mathbf{x}))\right] \tag{17}$$

where Σ_y is the noise covariance matrix and $|\Sigma_y|$ is its determinant. (Note that if the measurements are independent, this matrix is diagonal with the noise variance of the measurements in the diagonal elements of Σ_y.) Under these assumptions the posterior distribution turns out to be also a Gaussian process with mean and covariance functions given by[27]

$$\overline{f}(x^*) = \mathbf{k}^{\mathrm{T}}(x^*, \mathbf{x})(K(\mathbf{x}) + \Sigma_y)^{-1}\mathbf{y} \tag{18}$$

$$\begin{aligned} &\mathrm{cov}(f(x_1^*), f(x_2^*)) \\ &\quad = k(x_1^*, x_2^*) - \mathbf{k}^{\mathrm{T}}(x_1^*, \mathbf{x})(K(\mathbf{x}) + \Sigma_y)^{-1}\mathbf{k}(x_2^*, \mathbf{x}) \end{aligned} \tag{19}$$

where $\mathbf{k}(x^*, \mathbf{x})$ is the vector composed of covariance function values $\{k(x^*, x_i)\}$. For notational convenience and to keep our equations compact and readable later on, we shall often

dx.doi.org/10.1021/ct500438v | J. Chem. Theory Comput. XXXX, XXX, XXX−XXX

suppress the dependence on the observation locations $\mathbf{x}$ and write K_y for $K + \Sigma_y$, in line with ref 27. The posterior mean, $\overline{f}(x^*)$, (which coincides with the posterior mode and median) is often reported as the function reconstruction of the GPR model, while the diagonal elements of the posterior covariance function provide error bars.

According to eq 18 the prediction $\overline{f}(x^*)$ is simply a linear combination of kernel functions centered on the data points:[27]

$$\overline{f}(x^*) = \sum_{i=1}^{n} b_i k(x^*, x_i)$$

$$\mathbf{b} = (K(\mathbf{x}) + \Sigma_y)^{-1}\mathbf{y} \tag{20}$$

While this is not unlike a least-squares fit,[8] it differs in the way the coefficient vector $\mathbf{b}$ is calculated. In particular, through the presence of Σ_y GPR takes account of the noise associated with the data and, through the prior, of the similarity of data points, while the radial basis approach in its most basic form attempts to fit the data—regardless of its noise—exactly. As can be seen from eq 20, the covariance functions of GPR are analogous to the basis functions used in LSRBF (see Sec. 4.1), but the covariance has a statistical meaning, and this will play a significant role in what follows, in particular in how any free parameters are set.

The numerical implementation of GPR in the simplest case of noisy readings of function values is straightforward. From the sample positions, values, and noise, one precomputes a single 1-dimensional array $\mathbf{b}$:

1. Create an array of data positions $\{x_i\}$ and an array of corresponding data values $\{y_i\}$.
2. Compute the matrix K from data positions with $K_{ij} = k(x_i, x_j)$.
3. Evaluate the noise variance matrix Σ_y for the data values.
4. Compute the array $b_i = \sum_j (K + \sum_y)_{ij}^{-1} y_j$.

Evaluating the prediction of the model $\overline{f}(x^*)$ at an arbitrary position x^* just requires that one

1. Compute an array of covariances $K_i^* = k(x^*, x_i)$.
2. Compute the prediction $\overline{f}(x^*) = \sum_j K_i^* b_i$.

2.5. Covariance Functions and Hyperparameters: Prior Choices. The choice of covariance function determines how smooth the Gaussian process reconstruction will be. Many covariance functions have been proposed for the purpose of Gaussian process regression.[27] We have found the common choice of the squared exponential (SE) covariance function

$$k(x_1, x_2) = {\sigma_f}^2 \exp\left(-\frac{(x_1 - x_2)^2}{2l^2}\right) \tag{21}$$

to suffice for our purposes in this paper. It is infinitely differentiable an thus ensures a particularly smooth function reconstruction. We refer to it as a squared exponential (rather than Gaussian) in line with ref 27 in order to emphasize that this choice is not a prerequisite for Gaussian process regression and that other options are available. The name "Gaussian" in GPR refers to the probability distributions, rather than this choice of covariance function.

If we have the prior knowledge that the underlying function is periodic (e.g., the free energy corresponding to a dihedral angle), this should be reflected in the covariance function used. MacKay[36] has shown how this can be achieved for the SE and other covariance functions. The (periodic) variable x is first mapped onto a circle as $\mathbf{u}(x) = (\cos(x), \sin(x))$ and the covariance function then applied to $\mathbf{u}(x)$. For the SE covariance function one obtains

$$k_{2\pi}(x_1, x_2) = {\sigma_f}^2 \exp\left(-\frac{|\mathbf{u}(x_1) - \mathbf{u}(x_2)|^2}{2l^2}\right)$$

$$= {\sigma_f}^2 \exp\left(-\frac{2\sin^2\left(\frac{x_1 - x_2}{2}\right)}{l^2}\right) \tag{22}$$

We use this covariance function to treat dihedral angles in this paper. In two or more dimensions, as in sections 6.3 and 6.4, these expressions are generalized to

$$k_{2\pi}(x_1, x_2) = {\sigma_f}^2 \exp\left(-2\sum_\alpha \frac{\sin^2\left(\frac{x_{1,\alpha} - x_{2,\alpha}}{2}\right)}{{l_\alpha}^2} - \sum_\beta \frac{(x_{1,\beta} - x_{2,\beta})^2}{2l_\beta^2}\right) \tag{23}$$

where α and β are indices over periodic and nonperiodic collective coordinates, respectively, each of which can have its own length scale.

Finally, we note that these covariance functions contain a number of free parameters (commonly referred to as "hyperparameters" in the machine learning literature), such as the length scale l of the function to be inferred and the prior function variance ${\sigma_f}^2$, i.e. the expected variance of the function as a whole. Our view is that these are strictly part of the prior and should be informed by our prior knowledge of the system we investigate, rather than measured from the data itself. E.g. the meaning of l is the distance scale over which values of the unknown function are expected to become uncorrelated. The smoother we expect the reconstructed function to be, the larger l we should choose. Arguably in most free energy calculations we have a very good idea about the length and energy scales over which the free energy typically changes (e.g., the length and strength of a chemical bond, or simply π in the case of a bond or dihedral angle). Furthermore, we note that the effect of these choices on the reconstruction will become weak with increasing amounts of data. The same is not true for the noise covariance, Σ_y, since more precise measurements correspond to lower values and this relationship needs to be maintained.

3. BAYESIAN FREE ENERGY RECONSTRUCTION FROM HISTOGRAMS

We first illustrate the theory by the reconstruction of free energy profiles from histogram data. The basic idea is the following: For every umbrella window we construct a histogram consisting of b bins. Note that here the bins of the histograms do not have to be global, like in WHAM, but each umbrella window is associated with its own set of bins. We then calculate the unbiased free energies associated (approximately) with the bin centers (cf. section 2.1) up to an (unknown) additive constant which will vary from window to window. We account for the unknown constants by introducing them as new hyperparameters with an uninformative (i.e., flat) prior distribution and then integrate the posterior over all possible sets of values. Due to the use of Gaussian probability distributions, this integration step can be done analytically.

dx.doi.org/10.1021/ct500438v | J. Chem. Theory Comput. XXXX, XXX, XXX−XXX

3.1. Unknown Constants As Model Parameters. Writing $\mathbf{y}$ for the noisy free energy readings obtained, we have to modify the expression for the likelihood, eq 17, to allow for the unknown constants. There are as many unknowns as there are windows and we collect them in the vector $\mathbf{f}_0$. Given a total of n bins across all windows, let H be a matrix describing what window each bin belongs to: $H_{\theta i} = 1$, if bin i belongs to window θ and $H_{\theta i} = 0$ otherwise. Given $\mathbf{f}_0$, we can subtract it from the observed free energy readings and write down the following likelihood

$$\begin{aligned} p(\mathrm{y}|\mathbf{f}(\mathbf{x}), \mathbf{f}_0) &= p(\mathrm{y} - H^{\mathrm{T}}\mathbf{f}_0|\mathbf{f}(\mathbf{x})) \\ &= (2\pi)^{-n/2}\left|\Sigma_y\right|^{-1/2} \\ &\quad \times \exp\left[-\frac{1}{2}(\mathbf{y} - H^{\mathrm{T}}\mathbf{f}_0 - \mathbf{f}(\mathbf{x}))^{\mathrm{T}}\sum_y^{-1}\right. \\ &\quad \left.(\mathbf{y} - H^{\mathrm{T}}\mathbf{f}_0 - \mathbf{f}(\mathbf{x}))\right] \end{aligned} \tag{24}$$

To obtain the posterior distribution, we assume a Gaussian process prior on f and a flat (uninformative) prior on $\mathbf{f}_0$ and then integrate over $\mathbf{f}_0$. We defer the details of the derivation to Appendix A, where we obtain a posterior Gaussian process with mean

$$\begin{aligned} \overline{f}\,(x^*) &= \mathbf{k}^{\mathrm{T}}(x^*)\tilde{K}\mathbf{y} \\ \tilde{K} &= (K_y^{-1} - K_y^{-1}H^{\mathrm{T}}[HK_y^{-1}H^{\mathrm{T}}]^{-1}HK_y^{-1}) \end{aligned} \tag{25}$$

and covariance

$$\mathrm{cov}(f(x_1^*), f(x_2^*)) = k(x_1^*, x_2^*) - \mathbf{k}^{\mathrm{T}}(x_1^*)\tilde{K}\mathbf{k}(x_2^*) \tag{26}$$

The predictive mean and variance still have the forms of eqs 18 and 19, so the computational algorithm given in section 2.4 is thus easily adapted to the present case. The effective inverse covariance matrix, $\tilde{K}$, however, now shows a greater degree of complexity, accounting for our prior ignorance about the constants $\mathbf{f}_0$. The new term in eq 26 is positive, which makes sense: our ignorance about the free energy offsets translates into a broader posterior distribution. In Appendix B we show that the approach presented in this section is equivalent to using the ratio of the bin counts in all but one bin and the remaining bin in each window as input data to the GPR. This latter approach does not need the introduction and subsequent elimination of the unknown additive constants, since it only considers free energy *differences* within each window.

3.2. Modeling the Noise Structure in the Likelihood. The covariances in the previous sections were composed of two parts. The prior covariance matrix K results directly from the prior covariance function and the measurement positions x_i, but Σ_y, representing the noise associated with the input data needs to be estimated. We note that the GPR formalism necessitates modeling the noise as Gaussian in order to remain analytically tractable.

The noise associated with observations from two different windows will clearly be independent and the noise covariance matrix will thus have a block diagonal structure. Within one particular window the bin counts will have the covariance structure of a multinomial distribution. If all samples were independent this would simply be

$$\mathrm{cov}(n_{\theta i}, n_{\theta j}) = N_\theta(\delta_{ij}p_{\theta i} - p_{\theta i}p_{\theta j}) \tag{27}$$

where $p_{\theta i}$ are the bin probabilities in the *biased* simulation in window θ. To account for the time correlation in our samples, we need to consider the effective number of samples $N_{\theta,\mathrm{eff}}$, the number of (hypothetical) independent samples required to reproduce the information content of the N_θ correlated samples used.[37] This can be estimated, e.g., by a block averaging[38] procedure or an analysis of the time autocorrelation function.[37] Given that each effective sample corresponds to $N_\theta/N_{\theta,\mathrm{eff}}$ correlated samples, we obtain

$$\mathrm{cov}(n_{\theta i}, n_{\theta j}) = N_{\theta,\mathrm{eff}}\left(\frac{N_\theta}{N_{\theta,\mathrm{eff}}}\right)^2(\delta_{ij}p_{\theta i} - p_{\theta i}p_{\theta j}) \tag{28}$$

Recall that according to eq 11, up to constants not subject to noise, the observed bin free energies y_i, which form the input data for the Gaussian process regression, are obtained from the bin counts $n_{\theta i}$ as

$$y_i = -\frac{1}{\beta}\ln\frac{n_{\theta i}}{N_\theta} \tag{29}$$

Propagating errors to first order, we obtain the following estimator for the covariance

$$\begin{aligned} \mathrm{cov}(y_i, y_j) &\approx \frac{\partial y_i}{\partial n_{\theta i}}\mathrm{cov}(n_{\theta i}, n_{\theta j})\frac{\partial y_j}{\partial n_{\theta j}} \\ &= \frac{1}{N_{\theta,\mathrm{eff}}\beta^2}\left(\delta_{ij}\frac{N_\theta n_{\theta i}}{n_{\theta i}n_{\theta j}} - \frac{n_{\theta i}n_{\theta j}}{n_{\theta i}n_{\theta j}}\right) \\ &= \frac{1}{N_{\theta,\mathrm{eff}}\beta^2}\left(\delta_{ij}\frac{N_\theta}{n_{\theta i}} - 1\right) \end{aligned} \tag{30}$$

where we have also replaced $p_{\theta i}$ with its estimator $n_{\theta i}/N_\theta$.

3.3. Binning Algorithm. In this section we address the question of how to best construct the required histograms within each window. This problem is outside the scope of the Bayesian analysis presented above, where we have assumed the histogram as given. Generally speaking, fewer, larger bins will reduce the statistical noise, but many smaller bins would give more detailed information and minimize systematic errors due to associating the free energies obtained from the bin counts with the bin center.[39] The smoothing properties of our GPR procedure alleviate this trade-off to some extent, but cannot remove it completely. In the following paragraph we describe a binning algorithm we found to work well for the case of a harmonic umbrella potential. We use it throughout the rest of this paper.

To obtain the best possible statistics, we place our bins around the measured distribution mean μ in each window and within a range informed by the sample standard deviation σ. In our numerical examples we will use a range of $[\mu-3\sigma,\mu+3\sigma]$. Rather than splitting the histogram range into the required number of bins evenly, we found better results could be obtained by choosing bins that result in similar bin probabilities. We achieved this by choosing bin edges spaced by quantiles of a Gaussian with mean μ and variance σ^2. The advantage of choosing variable bin widths in this way is illustrated by the case of three bins: Three bins of equal width will result in a very accurate central reading and two very noisy readings from the tails. Upon taking differences (cf. Appendix B), this results in two even noisier difference readings. Three bins of approximately equal bin probability, on the other hand,

dx.doi.org/10.1021/ct500438v | J. Chem. Theory Comput. XXXX, XXX, XXX−XXX

will result in a somewhat noisier observation for the central bin, but the improvement in the tails will more than make up for this.

4. BAYESIAN FREE ENERGY RECONSTRUCTION FROM DERIVATIVE INFORMATION

Gaussian process regression is not restricted to function reconstructions from noisy function readings and in this section we describe how GPR may be used to reconstruct a free energy surface from a number of noisy observations of its gradient.

As mentioned above, for GPR to work analytically, both the prior and the likelihood need to be Gaussian. Therefore, observations that are linear functions of the function to be reconstructed are all admissible. Since differentiation is a linear operator, taking the derivative of a function modeled by a Gaussian process results in a new Gaussian process, obtained simply by applying the same operation to the mean and covariance functions.[27,40] For the covariance between values of the derivative and values of the function we thus have

$$k_{f,f'}(x_1, x_2) = \left\langle f(x_1)\frac{\partial}{\partial x_2}f(x_2)\right\rangle = \frac{\partial}{\partial x_2}\langle f(x_1)f(x_2)\rangle = \frac{\partial}{\partial x_2}k(x_1, x_2) \tag{31}$$

Similarly, the covariance between two derivative values can be obtained as

$$k_{f',f'}(x_1, x_2) = \frac{\partial^2}{\partial x_1 \partial x_2}k(x_1, x_2) \tag{32}$$

The posterior mean function given derivative information is then (cf. eq 18)

$$\overline{f}\,(x^*) = \mathbf{k}_{f,f'}^{\mathrm{T}}(x^*, \mathbf{x}')(K_{f',f'}(\mathbf{x}') + \Sigma_{y'})^{-1}\mathbf{y}' \tag{33}$$

where $\mathbf{y}'$ is the vector of (noisy) derivative data obtained at locations $\mathbf{x}'$ and $\Sigma_{y'}$ the associated noise covariance matrix. The posterior covariance, analogously to eq 19, is

$$\mathrm{cov}(f(x_1^*), f(x_2^*)) = k(x_1^*, x_2^*) - \mathbf{k}_{f,f'}^{\mathrm{T}}(x_1^*, \mathbf{x}')(K_{f',f'}(\mathbf{x}') + \Sigma_{y'})^{-1}\mathbf{k}_{f,f'}(x_2^*, \mathbf{x}') \tag{34}$$

Just as in the case of function observations (cf. section 2.4), we can again view the posterior mean as a linear combination of kernel functions centered on the data:

$$\overline{f}\,(x^*) = \sum_{i=1}^{n} b_i' k_{f,f'}(x^*, x_i') \tag{35}$$

where $\mathbf{b}' = (K_{f',f'}(\mathbf{x}') + \Sigma_{y'})^{-1}\mathbf{y}'$. Note, however, that the kernel functions are now different ($k_{f,f'}$ rather than the original covariance function k), reflecting the different nature of the observed data. The example of the SE covariance function, eq 21, illustrates this point clearly: when learning from function values, the reconstruction, eq 20, is a sum of Gaussians centered on the data points. When learning from derivatives, the reconstruction is a sum of differentiated Gaussians

$$k_{f,f'}(x^*, x_i') = \frac{\partial}{\partial x_i'}k(x^*, x_i') = \frac{x^* - x_i'}{l^2}\sigma_f^{\,2}\exp\left(-\frac{1}{2}\frac{(x^* - x_i')^2}{l^2}\right) \tag{36}$$

At the centers, $x^* = x_i'$, these functions are linear and evaluate to zero, which makes sense because the derivative data provide no direct information about absolute function values, only about linear changes.

We apply the technique to umbrella sampling by obtaining free energy derivatives via eq 15, but we stress that any scheme, such as thermodynamic integration[9,41] or ABF,[15] which reconstructs the free energy from its gradients can benefit from GPR.

In addition to estimating the free energy derivatives in each window, we also need to provide estimates for the noise in these observations. Just as in section 3.2, we again work with the assumption of Gaussian noise, and since the mean force in each window will be calculated from independent simulations, the noise covariance $\Sigma_{y'}$ is diagonal. We can therefore simply estimate its elements from the variances, $(\sigma_\theta^{\mathrm{b}})^2$, of the biased distributions. We obtain

$$\mathrm{var}(y_\theta') = \kappa_\theta^{\,2}\frac{(\sigma_\theta^{\mathrm{b}})^2}{N_{\theta,\mathrm{eff}}} \tag{37}$$

where y_θ' are the free energy derivatives estimated using eq 15 and $N_{\theta,\mathrm{eff}}$ is again the effective number of samples (cf. section 3.2).

Modifying the algorithm in section 2.4 is now straightforward, using the covariance in eq 32 when precomputing the $\mathbf{b}'$ array and the covariance in eq 31 when calculating the predicted mean. It is possible to extend the above formalism to incorporate second derivative information estimated from the observed sample variances, as suggested by Kästner and Thiel.[4] Since we did not find this to improve the quality of our reconstructions, probably because the noise associated with such readings is simply too large, we do not report any such results here.

4.1. Function Reconstruction Using Gradients in Several Dimensions: LSRBF vs GPR. We now consider the relationship between GPR as shown in the previous section and a least-squares fit using radial basis functions (LSRBF), in the multidimensional case. When reconstructing the free energy surface using a least-squares fit, it is written as a linear combination of basis functions centered on the data points,

$$f(\mathbf{x}^*) = \sum_{i=1}^{n} a_i k(\mathbf{x}^*, \mathbf{x}_i') \tag{38}$$

where $\{\mathbf{x}_i\}$ are the set of data locations (each is represented by a vector because we work in more than one dimension) and the coefficients, a_i, are obtained by minimizing the following error function, given by the sum of the squared deviations of the reconstructed gradients from the observed gradients

$$E(\mathbf{a}) = \sum_{i=1}^{n}\left|\sum_{j=1}^{n} a_j \nabla_{\mathbf{x}_i'} k(\mathbf{x}_i', \mathbf{x}_j') - \mathbf{y}_i'\right|^2 \tag{39}$$

where $\mathbf{y}_i'$ are the observed (noisy) free energy gradients. Like all least-squares problems, this minimization can be reduced to a linear algebraic system with the following solution:[6]

dx.doi.org/10.1021/ct500438v | J. Chem. Theory Comput. XXXX, XXX, XXX−XXX

$$\mathbf{a} = (\nabla\mathbf{k}^{\mathrm{T}}\nabla\mathbf{k})^{-1}\nabla\mathbf{k}^{\mathrm{T}}\mathbf{y}' \tag{40}$$

where $\mathbf{y}'$ is the vector obtained by concatenating all the measured gradients (such that $y'_{iD+\alpha}$ is the αth element of $\mathbf{y}'_i$, where D is the number of dimensions) and $\nabla\mathbf{k}$ is a $nD \times n$ matrix containing the gradients of all basis functions at all centers such that $(\nabla\mathbf{k})_{iD+\alpha,j}$ is the αth element of $\nabla_{\mathbf{x}'_i}k(\mathbf{x}'_i, \mathbf{x}'_j)$. Maragliano and Vanden-Eijnden further suggest optimizing the length scale (hyper-)parameter, l, by minimizing the residual $E(\mathbf{a})$.[6] We show below that this can lead to inferior results compared to setting a length-scale informed by our *a priori* knowledge about the system.

A comparison of eqs 35 and 38 shows that LSRBF and GPR use similar ansatzes but differ in the following important respects: the nature and number of the basis functions and the way the coefficients are calculated. The nature of the basis functions was addressed in the previous section. The difference in number of basis functions is unique to the multidimensional case: GPR uses one kernel function in the expansion for every component of the gradient data, rather than just one for each data point. The multidimensional analogue of eq 35 is thus

$$\bar{f}(\mathbf{x}^*) = \sum_{i=1}^{n}\sum_{\alpha=1}^{D} b_{i,\alpha}k_{f,f'_\alpha}(\mathbf{x}^*, \mathbf{x}'_i) \tag{41}$$

and the $nD \times nD$ covariance matrix is given by

$$[K_{f,f'}]_{iD+\alpha,jD+\beta} = \frac{\partial^2}{\partial x'_{i,\alpha}\partial x'_{j,\beta}}k(\mathbf{x}'_i, \mathbf{x}'_j) \tag{42}$$

The greater flexibility of GPR afforded by the increased number of basis functions leads to greater variational freedom, but the regularization due to the Bayesian prior mitigates the risk of overfitting. While the coefficients in the LSRBF approach are calculated to achieve the best possible fit of the data and therefore risk overfitting, GPR consistently takes account both of the noise associated with the input data through $\Sigma_{y'}$ and of the expected similarity of different data points through $K_{f',f'}$. Both approaches have a computational complexity that scales similarly with the number of data points, requiring the construction of a matrix involving gradients of the kernel, and the inversion of the matrix or the solution of a corresponding linear system.

4.2. Using Derivative Information together with Histograms. An advantage of working within a Bayesian framework is that different kinds of information can be brought together in a consistent manner. We can thus combine the approaches described in sections 3 and 4 to obtain a method which incorporates both the mean forces estimated in each window and the free energy estimates obtained from histograms in each window.

To achieve this we simply construct an extended covariance matrix between all function values (or function differences, cf. Appendix B) at $\mathbf{x}$ and all derivatives at $\mathbf{x}'$:

$$K_{f\oplus f'} = \begin{pmatrix} K(\mathbf{x}) & K_{f,f'}(\mathbf{x}, \mathbf{x}') \\ K^{\mathrm{T}}_{f,f'}(\mathbf{x}, \mathbf{x}') & K_{f',f'}(\mathbf{x}') \end{pmatrix} \tag{43}$$

In addition to the covariance matrices considered earlier, it also contains a block, $K_{ff'}(\mathbf{x},\mathbf{x}')$, with the covariances between function and derivative values; this block has elements $[K_{ff'}]_{ij} = k_{ff'}(x_i, x'_j)$, where $k_{ff'}$ was defined in section 4, eq 31.

We then make the approximation that the noise associated with the data obtained from our histograms is not correlated with the noise in the derivative readings. A combined noise matrix is then simply obtained by forming a block diagonal matrix, $\Sigma_{y\oplus y'} = \Sigma_y \oplus \Sigma_{y'}$, out of the original noise matrices. We also combine the data vectors $\mathbf{y}$ and $\mathbf{y}'$ of the two methods into a new, longer data vector, $\mathbf{y} \oplus \mathbf{y}'$ and the covariance vectors $\mathbf{k}(x, \mathbf{x})$ and $\mathbf{k}_{ff'}(x, \mathbf{x}')$ into the vector $\mathbf{k}_{f\oplus f'}(x) = \mathbf{k}(x, \mathbf{x}) \oplus \mathbf{k}_{ff'}(x, \mathbf{x}')$. Finally we also need to pad the H-matrix in these equations with a number of columns of zero-vectors equal to the number of derivative observations (to which the undetermined constants $\mathbf{f}_0$ do not apply). The difference formalism of Appendix B does, of course, again provide an alternative. We obtain a posterior by substituting these combined vectors and matrices for their counterparts in eqs 25 and 26, i.e. $K_{f\oplus f'} + \Sigma_{y\oplus y'}$ for K_y, $\mathbf{k}_{f,f\oplus f'}(x)$ for $\mathbf{k}(x)$, and $\mathbf{y} \oplus \mathbf{y}'$ for $\mathbf{y}$.

We have thus described three variants of the GPR method to reconstruct free energy profiles. Where we need to distinguish them, we shall refer to the methods, respectively, as GPR(h) for the purely histogram based approach of section 3, GPR(d) for the approach based on derivatives (section 4), and GPR(h+d) for the hybrid approach.

5. ERROR ESTIMATES

Gaussian process regression provides an estimate of the variance associated with the reconstruction. Care does, however, need to be exercised when this is interpreted in the present context. While taking the mean of the prior to be zero will result in a reconstructed profile that integrates to zero over its range (see below), we stress that the absolute values of the reconstructed free energies are meaningful only up to a global additive constant. The diagonals of the covariances calculated using eqs 26 or 34 must therefore not be interpreted as error bars on absolute free energy values. We can, however, use these equations legitimately to estimate the variance associated with free energy differences as

$$\begin{aligned}&\mathrm{var}[f(x_1^*) - f(x_2^*)] \\ &\quad = \mathrm{var}[f(x_1^*)] + \mathrm{var}[f(x_2^*)] - 2\mathrm{cov}[f(x_1^*), f(x_2^*)]\end{aligned} \tag{44}$$

Alternatively, we can reinterpret our reconstructed free energy values as differences from the global average (zero) value of the reconstruction and use the variance on these differences to obtain error bars. We distinguish two cases:

1. a translationally invariant, periodic covariance function, such as the one given in eq 22, $k_{2\pi}(x_1, x_2) = \tilde{k}_{2\pi}(x_1 - x_2) = \tilde{k}_{2\pi}(x_1 - x_2 + 2m\pi)$, where m is an integer
2. a translationally invariant covariance function which tends to 0 as $x_1 - x_2$ tends to $\pm\infty$, such as the SE covariance function of eq 21

and show in Appendix C that suitable error estimates are provided by the variances

$$\mathrm{var}[f(x^*)] - \frac{\bar{k}_{2\pi}}{2\pi} \tag{45}$$

and

$$\mathrm{var}[f(x^*)] \tag{46}$$

in the respective cases, where

dx.doi.org/10.1021/ct500438v | J. Chem. Theory Comput. XXXX, XXX, XXX−XXX

$$\bar{k}_{2\pi} = \int_0^{2\pi} \tilde{k}_{2\pi}(\tau)\, \mathrm{d}\tau \tag{47}$$

6. PERFORMANCE

We now compare the performance of our GPR reconstruction to those of WHAM and two variants of Umbrella Integration in one dimension, and to LSRBF and vFEP in two and four dimensions. The first UI variant is Kästner and Thiel's[4] original suggestion: the second derivative of the free energy is estimated in each window from the observed variance in the collective coordinate, $(\sigma_\theta^{\mathrm{b}})^2$, as

$$\frac{\partial^2 F_\theta(u)}{\partial u^2} \approx \frac{1}{\beta(\sigma_\theta^{\mathrm{b}})^2} - \kappa_\theta \tag{48}$$

Like the estimate for the first derivative, eq 15, this follows from the assumption that the free energy is locally (i.e., within each window) well approximated by a second order expansion.[4] The second derivatives are then used to linearly extrapolate the first derivatives in the vicinity of the observed means. In the second variant of UI we do not estimate second derivatives from the data but instead interpolate the mean forces from eq 15 using a cubic spline before integrating to yield the free energy profile.

6.1. Test Systems and Software. We shall now describe our test system, before explaining in more detail how we compare the performance of the various free energy reconstruction methods. The latter is not straightforward, because the performance of all methods is dependent on the choice of a set of parameters (number of windows, bias strength, number of bins), which we cannot expect to be optimal for all methods at once. In order to compare the methods in the most fair way, we want each to exhibit its best possible performance for a given total computational cost. It may be argued that in any particular application the optimal parameter settings are not known in advance, but we expect that in practice experience with each method and system guides the users' choice of parameters *a priori*, with only a small amount of system-specific tuning.

We used a model of alanine dipeptide (*N*-acetyl-alanine-*N*′-methylamide; Ace-Ala-Nme) to test our methods in one and two dimensions. Variants of this system have widely been used in the literature for similar purposes.[6,7,42] The molecule is modeled with the CHARMM22[43] force field in the gas-phase at a temperature of 300 K in the NVT ensemble, enforced by a Langevin thermostat[44] with a friction parameter of 100 fs. The equations of motion were integrated with a time step of 0.5 fs. The calculations were carried out with the LAMMPS[45] package augmented by the PLUMED[42] library. For the WHAM reconstructions reported in this paper, Alan Grossfield's code[46] has been used. The vFEP reconstructions were done with the publicly available software.[47]

Two slow degrees of freedom, the two backbone dihedral angles Φ (C−N−C_α−C) and Ψ (N−C_α−C−N), are present in this system. A one-dimensional system was obtained by adding a harmonic restraining potential in Φ to the system, centered at $\Phi = -2.0$ with a force constant of 100 kcal/mol, while using Ψ as the collective variable of interest. This choice yields a system where all complementary degrees of freedom are fast, so that problems with metastability are avoided. This may seem like a highly artificial one-dimensional system from a chemist's point of view, but it serves the purpose of testing a variety of free energy reconstruction methods. To obtain a converged reference free energy profile to which all methods are to be compared, we ran an umbrella sampling calculation consisting of 50 evenly spaced windows with a bias strength of κ = 100 kcal/mol. Within each window a trajectory was propagated for 50 ns from which samples were taken every 500 fs. A reference curve was constructed from this data such that the root-mean-square deviation between using different methods to construct the reference was less than $10^{-2}\ k_{\mathrm{B}}T$, more than precise enough for our purposes.

The collective variables in the two-dimensional test case are the two backbone dihedral angles. We collected data on an evenly spaced grid of 48 × 48 centers with bias strengths of κ = 50, 100, 200, and 400 kcal/mol in both collective variables and 500 ps-long trajectories at each center. As discussed in more detail below, all GPR and LSRBF results use κ = 100 kcal/mol, while both κ = 50 kcal/mol and κ = 200 kcal/mol are used for vFEP. All two-dimensional free energy reconstructions are performed using subsets of this data set, unless specifically stated otherwise.

To test the reconstruction in four dimensions we used the same simulation parameters, but replaced the dipeptide with alanine tripeptide (blocked dialanine, Ace-Ala-Ala-Nme) and used its four backbone dihedral angles as collective variables. We used two interlocking grids of 6^4 evenly spaced umbrella centers each (i.e., the second grid is obtained by translating the first by half a unit cell in all four directions) as well as a denser grid of 9^4 evenly spaced centers, all with a bias strength of κ = 400 kcal/mol and running trajectories of 500 ps at each center.

The sample noise increases with increasing umbrella strength (due to equipartition), but a stiffer umbrella also reduces the nonuniformity of the grid of mean sample positions, which are displaced from the umbrella centers by amounts proportional to the local gradients and inversely proportional to the umbrella strength. We find that in the four-dimensional case, when data is intrinsically more scarce, the stiffer bias potential gives better results than the softer one used in two dimensions.

For GPR we used a prior function variance of σ_f^2 = 10.0 kcal^2/mol^2 in the one-dimensional case but σ_f^2 = 20 kcal^2/mol^2 for the two and four-dimensional cases since there a larger range is expected. The length scale parameter was $l = \pi/3$ unless stated otherwise.

In the GPR and LSRBF approaches the periodicity of the reconstructed free energy profile is guaranteed through the use of a periodic covariance function (eq 22). In order to perform a fair comparison, we therefore must also enforce periodicity when testing other interpolation methods (UI in particular). We do this by linearly subtracting fractions of the integral over a full rotation

$$F(\Psi) = \int_0^{\Psi} F'_{\mathrm{UI}}(\tilde{\Psi})\, \mathrm{d}\tilde{\Psi} - \frac{\Psi}{2\pi} \int_0^{2\pi} F'_{\mathrm{UI}}(\tilde{\Psi})\, \mathrm{d}\tilde{\Psi} \tag{49}$$

where Ψ is a dihedral angle and F'_{UI} is the interpolated mean force from the umbrella simulations. This simple ad-hoc adjustment may be considered to be an extension of the original UI to periodic systems.[7]

GPR needs an estimate of the noise associated with each measurement, but especially for the shortest trajectories in two and more dimensions, the estimate of eq 37 evaluated for a single gradient may involve only a handful of samples, and therefore be inaccurate. Instead, for each trajectory length up to 5 ps, we use *all* the samples to estimate the error in the individual gradient sample, and use that value in the GPR for all gradient components.

dx.doi.org/10.1021/ct500438v | J. Chem. Theory Comput. XXXX, XXX, XXX−XXX

6.2. Performance in One Dimension. In order to select the best parameter settings for each reconstruction method we performed five sets of umbrella sampling calculations, each with 24 evenly distributed windows but differing bias strengths. Within each window we ran a 5 ns-long trajectory, recording samples every 50 fs. The data was then used to create repeated free energy reconstructions using a range of parameter choices and for different amounts of total trajectory used. The amount of data used was varied by factors of 10 from 12 ns per reconstruction (1/10 of the generated data) down to just 12 ps per reconstruction ($1/10^4$ of the available data). For each of these data amounts, the following parameters were varied and reconstructions produced for all cases:

- Umbrella strengths, κ: 5, 15, 25, 50, and 100 kcal/mol.
- Number of windows: 8, 12, and 24, while keeping the total data used constant by varying the trajectory length per window (we also checked using fewer windows, but these reconstructions were very clearly inferior).
- For WHAM and histogram-based GPR reconstructions, the number of bins: 20, 40, and 80 bins for WHAM (we deemed a reconstruction with fewer than 20 bins as too coarse to be meaningful, while significantly more than 80 bins resulted in very noisy reconstructions) and 2−10 bins per window for GPR(h) and GPR(h+d).

For each choice of method, total amount of data, and other parameters, 100 reconstructions were carried out using different sections of the full 5 ns trajectories. The root mean squared (RMS) error of these 100 reconstructions with respect to the reference curve was then calculated (in the case of WHAM at the bin centers only). Because all of the reconstructions are determined up to an additive constant only, this was chosen in each case to obtain a reconstruction with a global average value of zero. The optimal parameter settings for each method are summarized in Table 1. These best-case results were then used to compare the performance of the various methods with each other, as shown in Figure 1. Figure 2 shows representative reconstructions for some of the methods using different amounts of input data.

Table 1. Optimized Parameter Choices for a Number of Free Energy Reconstruction Methods Given Different Amounts of Total Sampling Time

		12 ns	1.2 ns	120 ps	12 ps
GPR (h+d)	κ	100	25	15	15
	win no.	12	24	24	8
	bin no.	5	2	2	2
GPR (h)	κ	25	15	15	15
	win no.	24	24	24	8
	bin no.	2	2	2	2
GPR (d)	κ	100	25	15	15
	win no.	24	24	24	12
UI spline	κ	100	25	15	25
	win no.	24	24	24	12
UI K and T	κ	15	15	15	15
	win no.	12	24	24	24
WHAM	κ	15	15	15	15
	win no.	24	24	24	24
	bin no.	20	20	20	20

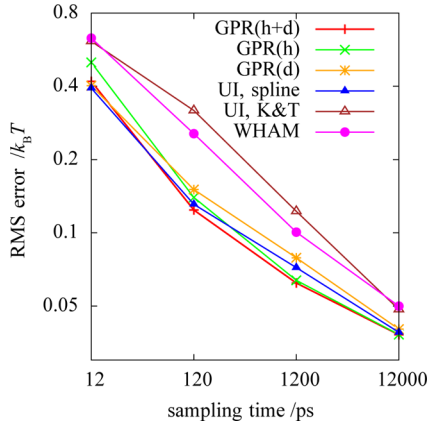

Figure 1. Comparison of the average root mean squared errors of a number of free energy reconstruction methods as a function of total sampling time using optimal parameter settings for each method and sampling time.

The traditional method rivalling the GPR reconstructions most closely in this comparative study is the spline based UI. We note that regression using one-dimensional cubic splines as basis functions can be thought of as a special case of Gaussian processes,[27] so a similar performance should perhaps not be very surprising. UI does not, however, allow for consistent treatment of measurement noise in the data. While in one dimension this does not seem to have a significant detrimental effect on the quality of the reconstructions as measured by the RMS error, the corresponding reconstructions in Figure 2 do seem to be less smooth than their GPR counterparts, with the example corresponding to the 12 ps trajectory even showing false local minima. The widely used WHAM is seen to produce very noisy reconstructions, which are improved upon by our approaches both visually and measurably in the RMS error.

Figure 1 also shows that Kästner and Thiel's[4] interpolation of mean forces—which uses measured second derivative information—performs rather less well than the spline interpolation which makes no reference to second derivatives. The reason for this is that the first and second derivative information enter the fit with a similar weight (particularly so if the windows are widely spaced), despite the fact that the latter typically has a much larger statistical error associated with it.

It is interesting to note that the optimal number of bins per window for GPR(h) and GPR(h+d) was two, independent of other parameters. We speculate that this is a result of the better statistics that can be achieved using fewer bins. Indeed, the situation has parallels to the estimation of free energies from derivatives. The information from a two-bin histogram is a single free energy difference, which is closely related to the information from a single free energy derivative, although without the approximation of the distribution mode by its mean (eq 15).

Finally, we observe that the methods based on mean force estimates from eq 15 (i.e., spline based UI and GPR(d)) slightly outperform the GPR reconstruction based on histograms only (GPR(h)) in the limit of very short sampling trajectories, while the opposite is true in the limit of long sampling. A tentative explanation is that in the abundant data regime statistical errors become small enough for systematic

dx.doi.org/10.1021/ct500438v | J. Chem. Theory Comput. XXXX, XXX, XXX−XXX

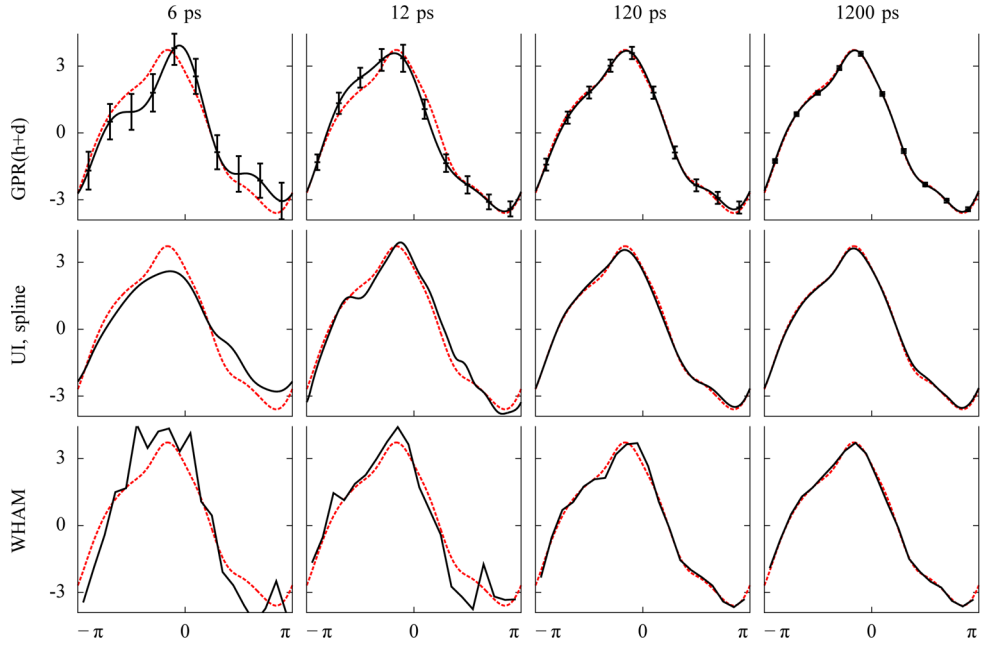

Figure 2. Representative free energy reconstructions (in units of k_BT) using different methods for total sampling times of 6, 12, 120, and 1200 ps. The dashed red curve is an accurate reference. The error bars for GPR(h+d) represent two standard deviations calculated using eq 80.

errors to dominate. Since eq 15 is based on a second order expansion of the free energy it introduces such a systematic error, which is apparently larger than the error made by constructing histograms. In the opposite regime statistical errors dominate, leading to two adverse effects for GPR(h). First, when using histograms, the data in each window have to be divided between at least two bins, whereas all data are used to obtain the estimate eq 15, thus resulting in better statistics. Furthermore, the assumption made in GPR(h) that the noise associated with the bin free energies can be approximated as Gaussian (cf. section 3.2), will start to break down in the limit of very short sampling trajectories. The hybrid GPR(h+d), finally, appears to fulfill our expectations of being the most accurate overall.

6.3. Two Dimensions. In two dimensions we compare GPR(d) to the established LSRBF method, and the recently proposed vFEP approach.[12,13] The latter models the underlying free energy with cubic splines and uses the maximum likelihood principle on the positions collected in all windows to optimize the spline parameters. It has been shown to significantly outperform both WHAM and MBAR, which also operate directly on the histogram, in two dimensions.[13]

In the following, where we report RMS errors with respect to the reference, we mainly compare *gradients* rather than the free energy profiles. This is because we prefer not to favor any of the reconstruction methods by selecting one to define the reference profile. The gradients, on the other hand, are direct outputs of the umbrella simulations, and can therefore be converged very accurately by running long simulations without the need for any postprocessing.

We first investigate the performance of the three methods as a function of grid size, i.e. the number of umbrella windows, using the entire 500 ps trajectory from each window in order to keep the statistical noise low. Figure 3 shows the RMS gradient error in the reconstruction of the two-dimensional free energy surface. The error is given as the mean squared deviation of the analytical gradients of each reconstruction from the measurements made on the densest (48 × 48) grid. We do find, as

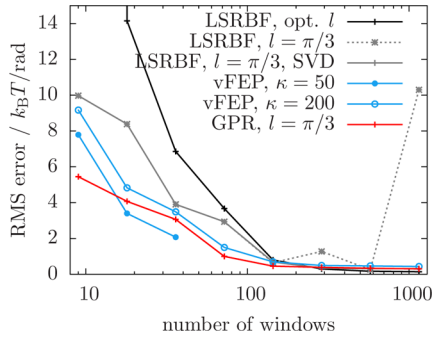

Figure 3. RMS deviations of free energy gradients of alanine dipeptide reconstructed using LSRBF (with and without singular value decomposition to control the condition number), vFEP (with two values of κ), and GPR(d).

expected, that the condition numbers of the matrices in the LSRBF reconstructions are often very large indeed, at times exceeding values of 10^{18}. This leads to an instability of the linear solver due to finite precision floating point arithmetic, which is easily controlled by employing a singular value decomposition (SVD), for which we use a relative threshold of 10^{-12}.

We also find that the publicly available vFEP implementation is very sensitive to the strength of the bias in the sampling. Data generated using a moderate spring constant of κ = 50 kcal/mol gave the best results when the grid was sparse, but on the denser grids we were unable to obtain a sensible reconstruction when attempting to process data that was generated using 50 and 100 kcal/mol, and only the data corresponding to κ = 200 kcal/mol was usable. Since κ is a parameter of the umbrella simulations themselves rather than that of the reconstruction, tuning it during the reconstruction process is not in general a practical option, because it would require rerunning the computationally expensive sampling. We therefore settle on one value, κ = 200 kcal/mol, for all vFEP results that follow in order to be sure that reconstructions can always be made. LSRBF and GPR(d) are much less sensitive to the umbrella

dx.doi.org/10.1021/ct500438v | J. Chem. Theory Comput. XXXX, XXX, XXX−XXX

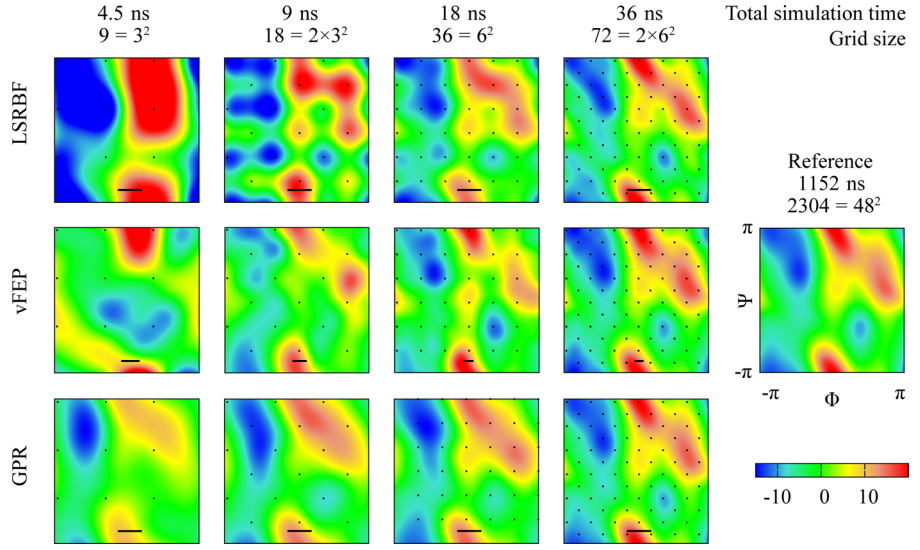

Figure 4. LSRBF, vFEP and GPR(d) reconstructions of the free energy surface (in units of k_BT) of alanine dipeptide in two dimensions using different numbers of windows, with a sampling trajectory of 500 ps/center. The LSRBF and GPR(d) reconstructions use κ = 100 kcal/mol, while vFEP use κ = 200 kcal/mol. The reconstructions are visually indistinguishable when more than 72 centers are used. The black dots mark the location of the bias centers. The black line segments indicate our choice of length-scale parameter $l = \pi/3$ for GPR(d) and LSRBF, and in the case of vFEP they show the spacing between spline points chosen by the vFEP software, corresponding to n_s = 8, 11, 15, 17, respectively.

strength. Higher values of κ help to reduce the systematic errors associated with the approximation in eq 15, but also lead to higher statistical noise and could potentially induce stiff dynamics that are hard to sample.

While the differences between the respective RMS gradient errors are not dramatic for the denser grids, in the regime of sparse grids both vFEP and GPR(d) outperform LSRBF. The visualizations of the free energy surface reconstructions, shown in Figure 4, underscore the advantages of GPR(d).

Figure 5 shows the variation of the RMS gradient error of GPR(d) and LSRBF with the choice of length scale parameter for two different grid sizes, as well as the variation of the square root of the quantity $E(\mathbf{a})$, defined in eq 39, which is used in ref 6 to find an "optimal" value for l for LSRBF. Optimizing the length-scale hyper-parameter l does not offer any great advantage over our *a priori* choice of $l = \pi/3$. Indeed it can lead to very unphysical results, particularly in the limit of scarce data in the LSRBF case, because it exacerbates the problem of overfitting. It is our view that for chemical and material systems it is usually not very difficult to choose a reasonable value of l before the reconstruction is undertaken, taking note of the meaning of this hyper-parameter: it is the expected correlation length of the free energy surface. For smooth functions in dihedral angles, setting it to any value in the range $[\pi/3, \pi]$ is reasonable, as demonstrated by the relatively flat curves of the RMS gradient error for l values in this range. We expect this to hold true for all free energy surfaces in dihedral angles of molecular systems.

We also show in Figure 5 the performance of vFEP as the number of spline points n_s is varied, which controls the smoothness of its reconstruction (in order to use the same horizontal scale, we made the identification $l = 2\pi/(n_s - 1)$. The error of the reconstruction changes significantly as n_s is varied, in contrast to the relative tolerance of LSRBF and GPR(d) with respect to their length scale parameters. Furthermore, the range of good parameters for the latter methods mostly depends on the properties of the underlying function, whereas the narrow range of n_s for which vFEP gives a good reconstruction varies with the grid density. The implementation of the vFEP method we used does offer a default choice for n_s, indicated by the gray dashed line, which

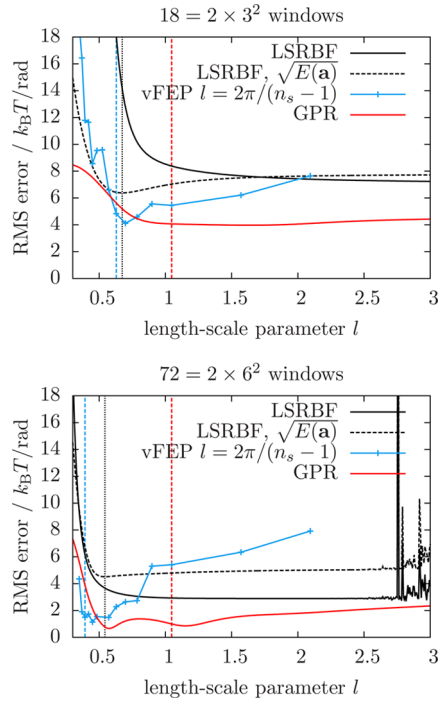

Figure 5. Variation of the RMS gradient error as a function of length scale for GPR(d), LSRBF, and vFEP, using 18 (top) and 72 (bottom) centers. For GPR(d) and LSRBF the length scale is the hyper-parameter l, while for vFEP we use the spacing between spline points. Also shown is the quantity $[E(\mathbf{a})]^{1/2}$ for the LSRBF reconstruction, used in ref 6 to optimize l; its minimum value is marked by the dotted black vertical line. The dashed red vertical line marks the value $l = \pi/3$. The dashed blue line corresponds to the automatic choice of spline point spacing of the vFEP implementation.

dx.doi.org/10.1021/ct500438v | J. Chem. Theory Comput. XXXX, XXX, XXX−XXX

seems to work well in the present case in which there is very little statistical noise in the data.

We now explore the relative performance of the methods in the regime of high statistical noise. To this end, we reconstructed the free energy surface from successively shorter trajectories sampled on a 12 × 12 grid of umbrella centers. As the trajectory length decreases, the results obtained show an increasing variance between runs. Figure 6 shows the medians

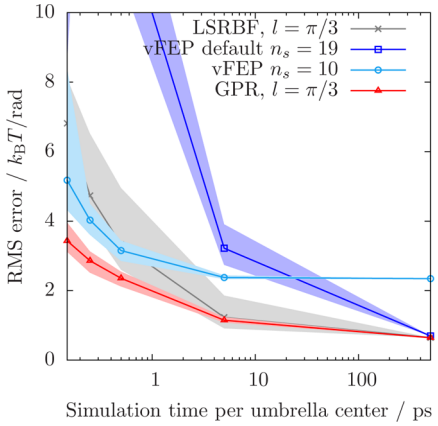

Figure 6. Median and typical range of the RMS deviations in the reconstructed free energy gradients of alanine dipeptide. Samples of 50 reconstructions for each trajectory length and method were used to calculate the median; the shaded area represents the range between the fifth and the 95th percentile of these samples (i.e., between the third best and third worst sample out of 50). All reconstructions use a grid of 12 × 12 windows, while the sampling time in each window is varied as shown.

of the RMS reconstruction gradient errors obtained from 50 different reconstructions with the same trajectory length. We also show an estimate of the breadth of the distribution, by plotting the range between the fifth and the 95th percentile of the sample of reconstructions.

In this regime of a dense grid and high noise the relative performance of vFEP and LSRBF are now opposite as compared with the previous low noise case. The vFEP method shows much worse degradation than LSRBF as the noise is increased, while GPR(d) outperforms both. Furthermore, while the performance of vFEP can be improved in the high noise limit by halving the number of spline points from the default choice (e.g., n_s = 10 instead of n_s = 19 for the plotted 12 × 12 grid) and forcing a smoother reconstruction, this reduction in variational freedom results less accurate reconstructions for the intermediate and low noise cases.

To give a feel for the kinds of reconstructions obtained, Figure 7 shows the reconstructions corresponding to approximately the 95th percentile of the sample (the third-worst out of 50) for each trajectory length. We show reconstructions from the worse end of the distribution as they better highlight the differences in resilience to noisy input data. While the LSRBF and vFEP reconstructions attempt to fit the data (including the noise) as closely as possible, the GPR(d) reconstructions are better in taking the statistical noise into account, resulting in a greater resilience to it. The flat green "reconstruction" of vFEP using data from only 0.15 ps trajectories corresponds to all zeros—there simply was not enough data there for the vFEP procedure to avoid converging to the null result.

So far we have showed reconstructions for various grid sizes at a fixed cost/grid point and also for varying trajectory length at a fixed grid size. But in practice one would be interested in the best reconstruction given a fixed total amount of computational cost, thus making a trade-off between more grid points or more samples collected at each point. Figure 8 shows the results combined for all grid sizes and trajectory lengths (note that the total simulation time on the x axis does not include any time needed for equilibration at each umbrella position). In order to attempt a fair comparison, we again halved the number of spline points compared to the default choice made by vFEP for short sampling times. For all grids and trajectory lengths we show the third worst reconstruction out of 50 samples.

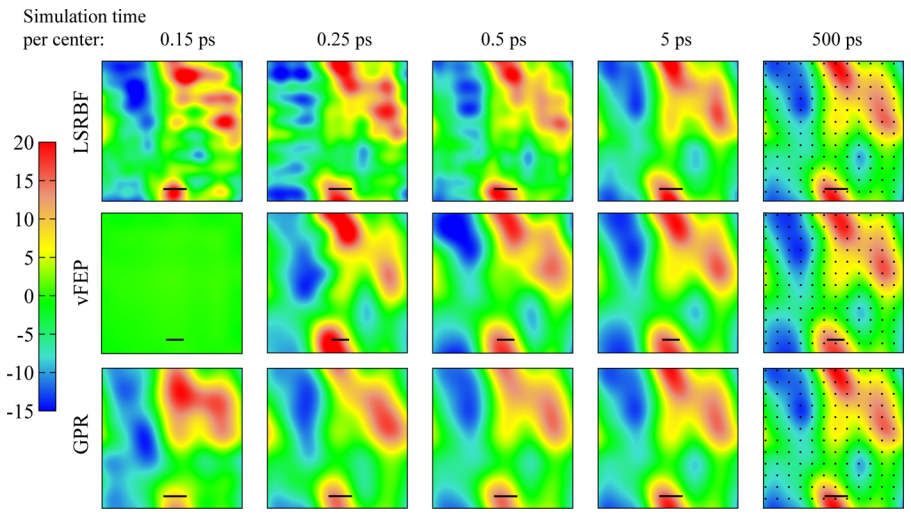

Figure 7. LSRBF, vFEP, and GPR(d) reconstructions of the free energy surface (in units of k_BT) of alanine dipeptide from data gathered in a 12 × 12 grid of windows over a varying amount of sampling time. The bias centers are marked by black dots in the rightmost column, but apply for all panels. We show the reconstructions with the third-largest RMS gradient errors from a sample of 50 (representing the 95th percentile) for each sampling time. The black line segments indicate the magnitude of the length-scale parameter $l = \pi/3$ for GPR(d) and LSRBF, and the spacing between the spline points for vFEP corresponding to n_s = 10 spline points.

dx.doi.org/10.1021/ct500438v | J. Chem. Theory Comput. XXXX, XXX, XXX−XXX

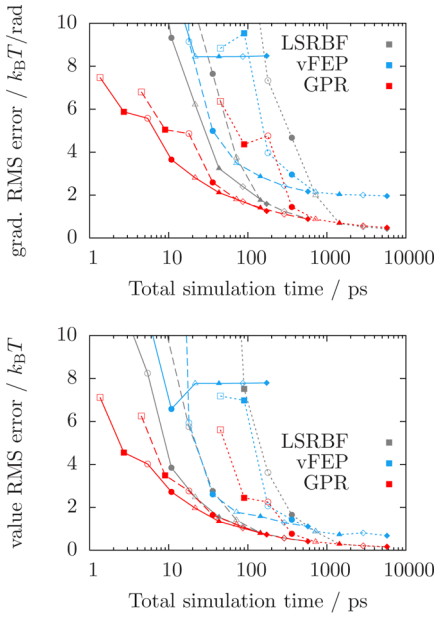

Figure 8. RMS error of gradient (top panel) and value (bottom panel) for vFEP (blue), RBF (gray), and GPR(d) (red) as a function of total amount of simulation time, for a variety of grids and trajectory lengths per grid point, showing the third worst result from a sample of 50 reconstructions. Line type indicates sampling time per window: 0.15 ps (solid), 0.5 ps (dashed), 5 ps (dotted). Symbol indicates grid size: 3 × 3 (open square), 3 × 3 × 2 (filled square), 6 × 6 (open cicle), 6 × 6 × 2 (filled circle), 12 × 12 (open triangle), 12 × 12 × 2 (filled triangle), 24 × 24 (open diamond), 24 × 24 × 2 (filled diamond).

Since it is not necessarily obvious what the error in the free energy will be as a function of the error in the gradient, here we plot both in two separate panels. The reference profile for the free energy error is the result of a GPR reconstruction based on all the data, i.e. 500 ps per window on the 48 × 48 grid.

Irrespective of the method used to do the reconstruction, it turns out to be always better to choose a denser grid and shorter trajectories, which is remarkable given the comparatively poor noise tolerance of LSRBF and vFEP. In a more realistic application, where equilibration time is included, the optimal trade-off is unclear. The use of denser grid would seem to require additional equilibration because each grid point needs to be equilibrated separately. However, if each grid point's trajectory is started from an adjacent one, the smaller distance from one grid point to the next might shorten the required equilibration time at each point.

6.4. Four Dimensions. Finally, we compare the performance of the LSRBF and GPR(d) methods in four dimensions, where data is necessarily much scarcer (the publicly available implementation of vFEP does not support more than two dimensions). Figure 9 shows the RMS deviations of free energy gradients obtained from reconstructions using various subsets of the data with respect to a reference obtained on the densest grid of 9^4 evenly spaced umbrella centers. GPR(d) outperforms the LSRBF fit, but even using more than 2000 windows GPR(d) has a remaining gradient error of about k_BT/rad. The LSRBF, on the other hand, fails to provide a reconstruction better than 10 k_BT/rad even when using the densest grid.

Figure 10 shows 2D slices of these reconstructions at values of −2.0 and 2.0 for the third and fourth backbone dihedral angles (counted from the N-terminal end), respectively. These slices are compared to a reference 2D reconstruction based on

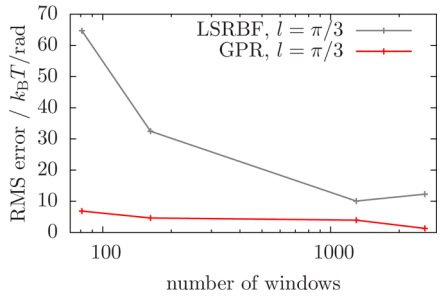

Figure 9. RMS deviations of free energy gradients reconstructed using LSRBF and GPR(d) in four dimensions from subsets of 2 × 6^4 free energy gradient observations, with respect to a reference set of 9^4 free energy gradients.

data sampled on a 2D grid of 48 × 48 centers in the same plane. For large numbers of centers both methods result in acceptable looking reconstructions. However, similarly to the case of reconstructing in two dimensions, only the GPR(d) fit remains qualitatively reasonable for small numbers of centers. The larger gradient error of the LSRBF reconstruction, especially for small numbers of centers as seen in Figure 9, is accompanied by prominent artifacts centered on the sampling points visible in Figure 10.

7. CONCLUSIONS

In this paper we showed how Gaussian process regression can be applied to the reconstruction of relative free energies from molecular dynamics trajectory data—histograms, mean restraint forces, or both—obtained in umbrella sampling simulations. It is a Bayesian method that explicitly takes into account the prior beliefs we have about the scale and smoothness of the free energy surface and consistently deals with statistical noise in the input data. Our GPR-based reconstruction can use information on the probability density from histograms in GPR(h), information on the free energy gradients in GPR(d), or both in GPR(h+d). It thus combines aspects of many previously published methods. GPR(h) is a density estimator, like WHAM, MBAR, vFEP, and GAMUS. GPR(d) on the other hand performs regression and integration on measurements of the free energy gradients, like UI and LSRBF. While MBAR, vFEP, WHAM, and LSRBF correspond to maximizing the likelihood, as a Bayesian method GPR maximizes the posterior and uses an explicit expression for the prior.

We have applied GPR and other reconstruction methods to the gas phase 1- and 2-dimensional free energy surfaces of the alanine dipeptide and the 4-dimensional free energy surface of the alanine tripeptide, using samples from molecular dynamics trajectories with quadratic restraining potentials centered on a uniform grid of points. We have demonstrated numerically that GPR leads to a small improvement in results when compared to widely used WHAM and UI methods in one dimension, and a large improvement compared to the LSRBF and vFEP methods in two and four dimensions. In one dimension the variant combining histograms and gradients performs best, although in the sparse data limit, where noise and systematic error most affect the histograms, the gradient-only variant is nearly as accurate. In higher dimensions, where it becomes increasingly harder to get enough data to fill in a histogram, we use only the gradient information. The advantage of GPR under these conditions is particularly apparent in the limits of short

dx.doi.org/10.1021/ct500438v | J. Chem. Theory Comput. XXXX, XXX, XXX−XXX

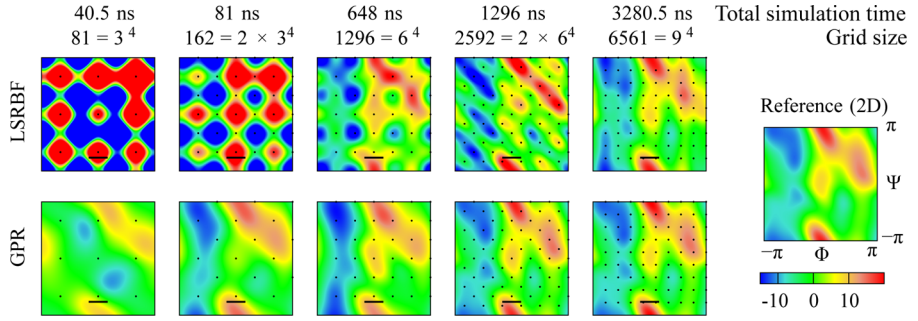

Figure 10. 2D slices of GPR(d) and LSRBF reconstructions of the 4D free energy surface (in units of k_BT) of alanine tripeptide using different numbers of windows, at third and fourth backbone dihedrals (from the N-terminus) of −2.0 and 2.0, respectively. Φ and Ψ refer to the first two backbone dihedrals from the N-terminus, respectively. The black dots mark the locations of the bias centers projected onto the 2D slice of the reconstruction. The black line segments indicate the magnitude of length-scale parameter $l = \pi/3$.

sampling trajectories (i.e., high statistical noise) and to some extent with sparse grids. This robustness to noise and weak sensitivity to the squared exponential kernel width hyperparameter are fundamental properties of the GPR approach, and are therefore expected to be transferable to free energy surface reconstruction in other systems. In cases where the free energy surface is expected to be less smooth, correspondingly less smooth covariance kernels may be used.

We argue that GPR represents the preferable, modern and practical approach to function fitting. It does not require any ad-hoc adjustments, rather the input parameters are intuitively meaningful and in realistic examples the results are insensitive to a broad range of choices. It provides meaningful error estimates with minimal extra computation. The framework allows for the simultaneous use of different types of information, such as bin counts and gradients.

The main benefit of using the GPR technique is that shorter trajectories can be used in mapping free energy profiles to acceptable accuracy. A reference software implementation for Gaussian process regression with the SE kernel for function reconstruction from gradient data in an arbitrary number of dimensions is freely available at www.libatoms.org.

APPENDIX A: DERIVATION OF THE GPR(H) POSTERIOR DISTRIBUTION

In this appendix we give details of the derivation of the predictive formulae stated in eqs 25 and 26 of section 3.1. We start from eq 24, a Gaussian likelihood allowing for a number of unknown constants $\mathbf{f}_0$. Given a set of such constants, we can simply view $\mathbf{y} - H^T\mathbf{f}_0$ as our data (which transforms eq 24 into the likelihood of the basic GPR case, eq 17) and thus use the standard predictive formulae, eqs 18 and 19 to obtain $p(f(x^*)|\mathbf{y}, \mathbf{f}_0)$ as a Gaussian process with the following mean and covariance functions:

$$\bar{f}(x^*) = \mathbf{k}^T(x^*)K_y^{-1}(\mathbf{y} - H^T\mathbf{f}_0) \tag{50}$$

$$\mathrm{cov}(f(x_1^*), f(x_2^*)) = k(x_1^*, x_2^*) - \mathbf{k}^T(x_1^*)K_y^{-1}\mathbf{k}(x_2^*) \tag{51}$$

To get from $p(f(x^*)|\mathbf{y},\mathbf{f}_0)$ to the desired $p(f(x^*)|\mathbf{y})$, we invoke some basic relations of conditional and joint probabilities:

$$\begin{aligned} p(f(x^*)|\mathbf{y}) &= \int p(f(x^*), \mathbf{f}_0|\mathbf{y})\, \mathrm{d}\mathbf{f}_0 \\ &= \int p(f(x^*)|\mathbf{y}, \mathbf{f}_0)p(\mathbf{f}_0|\mathbf{y})\, \mathrm{d}\mathbf{f}_0 \\ &= \frac{1}{p(y)} \int p(f(x^*)|\mathbf{y}, \mathbf{f}_0)p(\mathbf{y}|\mathbf{f}_0)p(\mathbf{f}_0)\, \mathrm{d}\mathbf{f}_0 \end{aligned} \tag{52}$$

We are interested in the case of an uninformative (i.e. constant) prior distribution $p(\mathbf{f}_0)$. Consequently, we can take this factor outside the integral and renormalize $p(f(x^*)|\mathbf{y})$ at the end. Similarly, the marginal likelihood of the model, $p(\mathbf{y}) = \int p(\mathbf{y}|\mathbf{f}_0)p(\mathbf{f}_0)\, \mathrm{d}\mathbf{f}_0$, is simply a normalization constant that we do not need to evaluate explicitly. Expressions for it can be found in ref 27. The remaining factor, $p(\mathbf{y}|\mathbf{f}_0)$, is the marginal likelihood of the model given a specific set of values for the unknown constants $\mathbf{f}_0$

$$p(\mathbf{y}|\mathbf{f}_0) = \int p(\mathbf{y}|\mathbf{f}, \mathbf{f}_0)p(\mathbf{f}|\mathbf{f}_0)\, \mathrm{d}\mathbf{f} \tag{53}$$

This integral is a convolution of two Gaussians, the prior, eq 16, and the likelihood, eq 24. It is a standard result that the convolution of two Gaussians is another Gaussian; the general case is given by

$$\begin{aligned} &\int \exp\left[-\frac{1}{2}(\mathbf{x}_1 - A\mathbf{x}_2 - \boldsymbol{\mu}_1)^T\Sigma_1^{-1}(\mathbf{x}_1 - A\mathbf{x}_2 - \boldsymbol{\mu}_1)\right]\exp\left[-\frac{1}{2}(\mathbf{x}_2 - \boldsymbol{\mu}_2)^T\Sigma_2^{-1}(\mathbf{x}_2 - \boldsymbol{\mu}_2)\right]\mathrm{d}\mathbf{x}_2 \\ &\propto \exp\left[-\frac{1}{2}(\mathbf{x}_1 - \boldsymbol{\mu}_1 - \boldsymbol{\mu}_2)^T(\Sigma_1 + A\Sigma_2A^T)^{-1}(\mathbf{x}_1 - \boldsymbol{\mu}_1 - A\boldsymbol{\mu}_2)\right] \end{aligned} \tag{54}$$

where $\mathbf{x}_1$ and $\boldsymbol{\mu}_1$ are vectors of size n, $\mathbf{x}_2$ and $\boldsymbol{\mu}_2$ vectors of size m, and Σ_1 and Σ_2 are symmetric positive definite matrices of sizes $n \times n$ and $m \times m$, respectively.

In the present case A is the identity, and thus we may simply add the means (zero for the prior and $H^T\mathbf{f}_0$ for the likelihood) and covariance matrices (K and Σ_y) to obtain

$$p(\mathbf{y}|\mathbf{f}_0) \propto |K_y|^{-1/2}\exp\left[-\frac{1}{2}(\mathbf{y} - H^T\mathbf{f}_0)^TK_y^{-1}(\mathbf{y} - H^T\mathbf{f}_0)\right] \tag{55}$$

Returning to eq 52, we can now see that the posterior distribution sought, $p(f(x^*)|\mathbf{y})$, is, up to normalization, yet another convolution: a convolution of the posterior Gaussian

dx.doi.org/10.1021/ct500438v | J. Chem. Theory Comput. XXXX, XXX, XXX−XXX

process given $\mathbf{f}_0$, $p(f(x^*)|\mathbf{y},\mathbf{f}_0)$, and the marginal likelihood $p(\mathbf{y}|\mathbf{f}_0)$. To apply eq 54 once more, we first need to reexpress $p(\mathbf{y}|\mathbf{f}_0)$, eq 55, as a Gaussian in $\mathbf{f}_0$ rather than in $\mathbf{y}$. Expanding the product and completing the square yields

$$\log p(\mathbf{y}|\mathbf{f}_0) = -\frac{1}{2}(\mathbf{f}_0 - \bar{\mathbf{f}}_0)^{\mathrm{T}}[HK_y^{-1}H^{\mathrm{T}}](\mathbf{f}_0 - \bar{\mathbf{f}}_0) - \frac{1}{2}\mathbf{y}^{\mathrm{T}}K_y^{-1}\mathbf{y} + \frac{1}{2}\mathbf{y}^{\mathrm{T}}K_y^{-1}H^{\mathrm{T}}[HK_y^{-1}H^{\mathrm{T}}]^{-1}HK_y^{-1}\mathbf{y} - \frac{1}{2}\log|K_y| + \text{const} \tag{56}$$

where $\bar{\mathbf{f}}_0 = [HK_y^{-1}H^{\mathrm{T}}]^{-1}HK_y^{-1}\mathbf{y}$. Only the first term depends on $\mathbf{f}_0$; we can ignore the others as normalization constants. We can now bring together eqs 52, 54, 50, 51, and 56 to obtain eqs 25 and 26 as the mean and covariance functions for the posterior Gaussian process $p(f|\mathbf{y})$.

APPENDIX B: ALTERNATIVE FORMULATION OF GPR(H)—LEARNING FROM FINITE DIFFERENCES

In this appendix we present an alternative, but entirely equivalent, formulation of the method presented in section 3. We can eliminate the unknown constants $\mathbf{f}_0$ by using free energy differences rather than absolute free energies as input data. More specifically, in each window with b bins we can use the differences of the free energies in $b - 1$ bins and the remaining bin. We first spell out the details of this alternative approach, before demonstrating its equivalence to the view taken earlier.

The free energy differences, $\Delta\mathbf{y}$, to be used as input data can be obtained from the bin free energies, $\mathbf{y}$, of section 3 by applying a difference operator B_Δ, i.e.

$$\Delta\mathbf{y} = B_\Delta\mathbf{y} \tag{57}$$

where the (rectangular) matrix B_Δ has a block-diagonal structure with each $b - 1 \times b$ entry block.

$$B_\Delta^w = \begin{pmatrix} 1 & 0 & \cdots & 0 & -1 \\ 0 & 1 & \ddots & \vdots & -1 \\ \vdots & \ddots & \ddots & 0 & \vdots \\ 0 & \cdots & 0 & 1 & -1 \end{pmatrix} \tag{58}$$

i.e. the identity matrix extended by a column of -1 entries, for every window. In this form, the final bin of each window is assigned to be the reference bin with respect to which the differences of the free energies of the remaining bins are evaluated. A different choice of reference bin would simply shift the position of the (now) rightmost column of B_Δ^w. As will become clear from what follows, the choice of reference bin is entirely arbitrary and does not affect the result.

Using $\Delta\mathbf{y}$ as input data in GPR we obtain the following posterior distribution:

$$\bar{f}(x^*) = \mathbf{k}_\Delta^{\mathrm{T}}(x^*)K_{\Delta_y}^{-1}\Delta\mathbf{y} = \mathbf{k}^{\mathrm{T}}(x^*)B_\Delta^{\mathrm{T}}(B_\Delta K_y B_\Delta^{\mathrm{T}})^{-1}B_\Delta\mathbf{y} \tag{59}$$

$$\mathrm{cov}(f(x_1^*), f(x_2^*)) = k(x_1^*, x_2^*) - \mathbf{k}_\Delta^{\mathrm{T}}(x_1^*)K_{\Delta_y}^{-1}\mathbf{k}_\Delta(x_2^*) = k(x_1^*, x_2^*) - \mathbf{k}^{\mathrm{T}}(x_1^*)B_\Delta^{\mathrm{T}}(B_\Delta K_y B_\Delta^{\mathrm{T}})^{-1}B_\Delta\mathbf{k}(x_2^*) \tag{60}$$

where $\mathbf{k}(x^*)$, $K_y = K + \Sigma_y$ and $\mathbf{y}$ are the same as in section 3 and we have written $\mathbf{k}_\Delta(x^*) = B_\Delta\mathbf{k}(x^*)$ and $K_{\Delta_y} = B_\Delta K_y B_\Delta^{\mathrm{T}} = B_\Delta K B_\Delta^{\mathrm{T}} + B_\Delta\Sigma_y B_\Delta^{\mathrm{T}}$.

To show the equivalence of this with respect to the posterior distribution derived in section 3, we first note that eqs 59 and 60 will coincide with eqs 25 and 26 if the following holds:

$$B_\Delta^{\mathrm{T}}(B_\Delta K_y B_\Delta^{\mathrm{T}})^{-1}B_\Delta \stackrel{?}{=} K_y^{-1} - K_y^{-1}H^{\mathrm{T}}[HK_y^{-1}H^{\mathrm{T}}]^{-1}HK_y^{-1} \tag{61}$$

In order to prove this relation we shall find it useful to consider first the simplified case obtained by replacing B_Δ with a truncated identity matrix I_{-w}, obtained from the $n \times n$ identity by removing a number w of rows from the bottom to give an $(n - w) \times n$ matrix. In the context of GPR we might interpret this as making use of only the first $n - w$ of n data points. Multiplication of an $n \times x$ matrix from the left with I_{-w} thus removes the bottom w rows of this matrix, while multiplication of an $x \times n$ matrix from the right with I_{-w}^{T} removes its rightmost w columns. Similarly, multiplication of an $(n - w) \times x$ matrix from the left with I_{-w}^{T} will add w rows of zeros and multiplication of an $x \times (n - w)$ matrix from the right with I_{-w} will add w columns of zeros. The expression $I_{-w}^{\mathrm{T}}(I_{-w}K_yI_{-w}^{\mathrm{T}})^{-1}I_{-w}$ thus describes the matrix obtained by inverting the top-left $(n - w) \times (n - w)$ block of K_y and padding the result with zeros to restore its size to $n \times n$. To carry on, we need to invoke a standard result (cf. e.g. ref 27) about the inverse of a partitioned matrix: Given an invertible matrix A and its inverse, we may partition both matrices in the same way and write

$$A^{-1} = \begin{pmatrix} P & Q \\ R & S \end{pmatrix}^{-1} = \begin{pmatrix} \tilde{P} & \tilde{Q} \\ \tilde{R} & \tilde{S} \end{pmatrix} \tag{62}$$

where P, $\tilde{P}$, S, and $\tilde{S}$ are square matrices. The basic result we need is

$$P^{-1} = \tilde{P} - \tilde{Q}\tilde{S}^{-1}\tilde{R} \tag{63}$$

which we extend for our purposes to

$$\begin{pmatrix} P^{-1} & 0 \\ 0 & 0 \end{pmatrix} = A^{-1} - \begin{pmatrix} \tilde{Q} \\ \tilde{S} \end{pmatrix}\tilde{S}^{-1}(\tilde{R} \quad \tilde{S}) \tag{64}$$

As explained above, the matrix I_{-w} can be used to choose the top left block of a matrix. In order to use eq 64 we need to define the complementary $n \times w$ matrix H_w, capable of selecting the bottom right block. This is precisely the matrix removed from the identity in order to obtain I_{-w}, i.e.

$$I = \begin{pmatrix} I_{-w} \\ H_w \end{pmatrix} \tag{65}$$

We can thus apply eq 64 to our simplified problem and obtain

$$I_{-w}^{\mathrm{T}}(I_{-w}K_yI_{-w}^{\mathrm{T}})^{-1}I_{-w} = K_y^{-1} - K_y^{-1}H_w^{\mathrm{T}}[H_wK_y^{-1}H_w^{\mathrm{T}}]^{-1}H_wK_y^{-1} \tag{66}$$

which is already very close in form to eq 61. To generalize this result we first note that B_Δ may be written in terms of a larger, $n \times n$ matrix B as

$$B_\Delta = I_{-w}B \tag{67}$$

dx.doi.org/10.1021/ct500438v | J. Chem. Theory Comput. XXXX, XXX, XXX−XXX

where the first $n - w$ rows of B are the same as B_Δ. We choose the additional rows to be the same as the rows of the matrix H, defined in section 3, i.e.

$$H_w B = H \tag{68}$$

Crucially for what follows, these extra rows are both mutually orthogonal as well as orthogonal to the rows of B_Δ. This will allow us to write

$$H_w (B^{-1})^{\mathrm{T}} = \mathrm{diag}(\mathbf{h})^{-2} H_w B = \mathrm{diag}(\mathbf{h})^{-2} H \tag{69}$$

where the diagonal matrix $\mathrm{diag}(\mathbf{h})$ contains the vector norms of the rows of the matrix H. (For example, a row in H corresponding to a window with b bins, will have norm $\sqrt{b}$.)

We can thus write

$$\begin{aligned} &B_\Delta^{\mathrm{T}} (B_\Delta K_y B_\Delta^{\mathrm{T}})^{-1} B_\Delta = B^{\mathrm{T}} I_{-w}^{\mathrm{T}} (I_{-w} B K_y B^{\mathrm{T}} I_{-w}^{\mathrm{T}})^{-1} I_{-w} B \\ &= B^{\mathrm{T}} (B^{\mathrm{T}})^{-1} K_y^{-1} B^{-1} B - B^{\mathrm{T}} (B^{\mathrm{T}})^{-1} K_y^{-1} B^{-1} H_w^{\mathrm{T}} \\ &\quad [H_w (B^{\mathrm{T}})^{-1} K_y^{-1} B^{-1} H_w^{\mathrm{T}}]^{-1} H_w (B^{\mathrm{T}})^{-1} K_y^{-1} B^{-1} B \\ &= K_y^{-1} - K_y^{-1} H^{\mathrm{T}} \mathrm{diag}(\mathbf{h})^{-2} \\ &\quad [\mathrm{diag}(\mathbf{h})^{-2} H K_y^{-1} H^{\mathrm{T}} \mathrm{diag}(\mathbf{h})^{-2}]^{-1} \mathrm{diag}(\mathbf{h})^{-2} H K_y^{-1} \\ &= K_y^{-1} - K_y^{-1} H^{\mathrm{T}} [H K_y^{-1} H^{\mathrm{T}}]^{-1} H K_y^{-1} \end{aligned} \tag{70}$$

where the second equality is obtained by invoking eq 66 with BK_yB^{T} now replacing K_y.

This completes the proof of eq 61. Using free energy differences in GPR is thus equivalent to introducing the undetermined constants $\mathbf{f}_0$. This also demonstrates that the choice of reference bin is indeed arbitrary and does not affect the result. Indeed, any operator B_Δ, with rows that are mutually linearly independent and orthogonal to the rows of H, will give this same result.

APPENDIX C: DERIVATION OF THE ERROR ESTIMATES

In this appendix we derive error estimates of the Gaussian process for the free energy differences in the periodic and nonperiodic cases.

In the first case the reconstruction repeats itself periodically and we start by showing that the predicted mean of the reconstruction averages to zero across the whole period, i.e.

$$\int_0^{2\pi} \bar{f}(x^*)\, \mathrm{d}x^* = 0 \tag{71}$$

In the case of GPR(h) (eq 25) this expands to

$$\int_0^{2\pi} \bar{f}(x^*)\, \mathrm{d}x^* = \left[\int_0^{2\pi} k^{\mathrm{T}}(x^*)\, \mathrm{d}x^*\right] (K_y^{-1} - K_y^{-1} H^{\mathrm{T}} [H K_y^{-1} H^{\mathrm{T}}]^{-1} H K_y^{-1}) \mathbf{y} \tag{72}$$

The vector $\mathbf{k}(x^*)$ comprises the prior covariances between the function at x^* and the location of the data $\mathbf{x}$, i.e. its elements are $(\mathbf{k}(x^*))_i = k_{2\pi}(x^*, x_i)$. Because of the translational invariance of the covariance function, these integrals do not depend on the location of the training data, i.e.

$$\bar{k}_{2\pi} = \int_0^{2\pi} k_{2\pi}(x^*, x_i)\, \mathrm{d}x^* = \int_0^{2\pi} \tilde{k}_{2\pi}(\tau)\, \mathrm{d}\tau \tag{73}$$

and we have

$$\int_0^{2\pi} \bar{f}(x^*)\, \mathrm{d}x^* = \bar{k}_{2\pi} \mathbf{1}^{\mathrm{T}} (K_y^{-1} - K_y^{-1} H^{\mathrm{T}} [H K_y^{-1} H^{\mathrm{T}}]^{-1} H K_y^{-1}) \mathbf{y} \tag{74}$$

where $\mathbf{1}$ is a vector with all elements equal to 1. From the result of Appendix B it follows, however, that $\mathbf{1}^{\mathrm{T}}(K_y^{-1} - K_y^{-1} H^{\mathrm{T}} [H K_y^{-1} H^{\mathrm{T}}]^{-1} H K_y^{-1})$ is equal to the zero vector and so we obtain eq 71. In the case of GPR(d) (eq 33), we get

$$\int_0^{2\pi} \bar{f}(x^*)\, \mathrm{d}x^* = \left[\int_0^{2\pi} k_{f,f'}^{\mathrm{T}}(x^*)\, \mathrm{d}x^*\right] (K_{f',f'}(\mathbf{x}') + \Sigma_{y'})^{-1} \mathbf{y}' \tag{75}$$

The vector $\mathbf{k}_{ff'}(x^*)$ has elements (eq 31)

$$k_{f,f'}(x^*, x_i') = \frac{\partial}{\partial x_i'} k_{2\pi}(x^*, x_i') = -\frac{\partial}{\partial x^*} k_{2\pi}(x^*, x_i') \tag{76}$$

where the second equality is a direct consequence of the translational invariance of the covariance function. Integrating these covariance functions over x^* thus gives 0 for all x'_i and eq 71 immediately follows. The above arguments are virtually the same in the case of a covariance function of our second type, and we get

$$\lim_{\Delta \to \infty} \frac{1}{2\Delta} \int_{-\Delta}^{\Delta} \bar{f}(x^*)\, \mathrm{d}x^* = 0 \tag{77}$$

in this case.

To obtain error bars on the reconstructed free energy profile for periodic and nonperiodic collective variables, we need to find expressions for

$$\mathrm{var}\left[f(x^*) - \frac{1}{2\pi} \int_0^{2\pi} f(x_1^*)\, \mathrm{d}x_1^*\right] \tag{78}$$

and

$$\mathrm{var}\left[f(x^*) - \lim_{\Delta \to \infty} \frac{1}{2\Delta} \int_{-\Delta}^{\Delta} f(x_1^*)\, \mathrm{d}x_1^*\right] \tag{79}$$

respectively, depending on the covariance function used. Note the presence of the full posterior f in the above integrals, rather than the posterior mean $\bar{f}$. We are now going to show that suitable error estimates are provided by

$$\mathrm{var}\left[f(x^*) - \frac{1}{2\pi} \int_0^{2\pi} f(x_1^*)\, \mathrm{d}x_1^*\right] = \mathrm{var}[f(x^*)] - \frac{\bar{k}_{2\pi}}{2\pi} \tag{80}$$

for the periodic case, and

$$\mathrm{var}\left[f(x^*) - \lim_{\Delta \to \infty} \frac{1}{2\Delta} \int_{-\Delta}^{\Delta} f(x_1^*)\, \mathrm{d}x_1^*\right] = \mathrm{var}[f(x^*)] \tag{81}$$

for the non-periodic case.

In the periodic case we obtain

dx.doi.org/10.1021/ct500438v | J. Chem. Theory Comput. XXXX, XXX, XXX−XXX

$$\mathrm{var}\left[f(x^*) - \frac{1}{2\pi}\int_0^{2\pi} f(x_1^*)\,\mathrm{d}x_1^*\right] = \mathrm{var}[f(x^*)] + \mathrm{var}\left[\frac{1}{2\pi}\int_0^{2\pi} f(x_1^*)\,\mathrm{d}x_1^*\right] - 2\mathrm{cov}\left[f(x^*), \frac{1}{2\pi}\int_0^{2\pi} f(x_1^*)\,\mathrm{d}x_1^*\right] = \mathrm{var}[f(x^*)] + \frac{1}{(2\pi)^2}\int_0^{2\pi}\int_0^{2\pi} \mathrm{cov}[f(x_1^*), f(x_2^*)]\,\mathrm{d}x_1^*\,\mathrm{d}x_2^* - \frac{2}{2\pi}\int_0^{2\pi} \mathrm{cov}[f(x^*), f(x_1^*)]\,\mathrm{d}x_1^* \quad (82)$$

In the case of GPR(h) we can expand the double integral as follows (cf. eq 26):

$$\begin{aligned}
&\int_0^{2\pi}\int_0^{2\pi} \mathrm{cov}[f(x_1^*), f(x_2^*)]\,\mathrm{d}x_1^* dx_2^* \\
&= \int_0^{2\pi}\int_0^{2\pi} k_{2\pi}(x_1^*, x_2^*)\,\mathrm{d}x_1^*\,\mathrm{d}x_2^* \\
&- \sum_{ij}\kappa_{ij}\left(\int_0^{2\pi} k_{2\pi}(x_i, x_1^*)\,\mathrm{d}x_1^*\right)\left(\int_0^{2\pi} k_{2\pi}(x_j, x_2^*)\,\mathrm{d}x_2^*\right) \\
&= 2\pi\bar{k}_{2\pi} - \bar{k}_{2\pi}^2\mathbf{1}^{\mathrm{T}}\kappa\mathbf{1} \\
&= 2\pi\bar{k}_{2\pi}
\end{aligned} \quad (83)$$

where κ denotes the matrix $K_y^{-1} - K_y^{-1}H^{-1}[HK_y^{-1}H^{\mathrm{T}}]^{-1}HK_y^{-1}$, and we have again used the result that $\mathbf{1}^{\mathrm{T}}\kappa = 0$. Similarly

$$\int_0^{2\pi} \mathrm{cov}[f(x^*), f(x_1^*)]\,\mathrm{d}x_1^* = \bar{k}_{2\pi} \quad (84)$$

and we obtain eq 80

$$\mathrm{var}\left[f(x^*) - \frac{1}{2\pi}\int_0^{2\pi} f(x_1^*)\,\mathrm{d}x_1^*\right] = \mathrm{var}[f(x^*)] - \frac{\bar{k}_{2\pi}}{2\pi}$$

It is straightforward to show that this result also holds for GPR(d). One simply expands the integrals of eq 82 using eq 34 and all integrals involving differentiated covariance functions evaluate to zero (cf. eq 76), leaving eq 80.

Again, a very similar line of reasoning can be employed for our second type of covariance function, though the diverging denominator provides an obvious shortcut in this case. It is also because of this diverging denominator (compared to the finite value of 2π in the first case) that the final result, eq 81, is even simpler:

$$\mathrm{var}\left[f(x^*) - \lim_{\Delta\to\infty}\frac{1}{2\Delta}\int_{-\Delta}^{\Delta} f(x_1^*)\,\mathrm{d}x_1^*\right] = \mathrm{var}[f(x^*)]$$

AUTHOR INFORMATION

Corresponding Authors

*E-mail: thomas.stecher@tum.de (T.S.).

*E-mail: gc121@cam.ac.uk (G.C.).

Funding

N.B. acknowledges funding for this project by the Office of Naval Research (ONR) through the Naval Research Laboratory's basic research program. G.C. acknowledges support from the Office of Naval Research under Grant No. N000141010826 and from the European Union FP7-NMP programme under Grant No. 229205 "ADGLASS".

Notes

The authors declare no competing financial interest.

ACKNOWLEDGMENTS

We thank Eric Vanden-Eijnden for comments on the manuscript.

REFERENCES

(1) Torrie, G. M.; Valleau, J. P. *Chem. Phys. Lett.* **1974**, *28*, 578−581.
(2) Kumar, S.; Bouzida, D.; Swendsen, R. H.; Kollman, P. A.; Rosenberg, J. M. *J. Comput. Chem.* **1992**, *13*, 1011−1021.
(3) Souaille, M.; Roux, B. *Comput. Phys. Commun.* **2001**, *135*, 40−57.
(4) Kästner, J.; Thiel, W. *J. Chem. Phys.* **2005**, *123*, 144104.
(5) Kästner, J.; Thiel, W. *J. Chem. Phys.* **2006**, *124*, 234106.
(6) Maragliano, L.; Vanden-Eijnden, E. *J. Chem. Phys.* **2008**, *128*, 184110.
(7) Kästner, J. *J. Chem. Phys.* **2009**, *131*, 034109.
(8) Buhmann, M. D. *Acta Numerica* **2000**, *9*, 1−38.
(9) Kirkwood, J. G. *J. Chem. Phys.* **1935**, *3*, 300−313.
(10) Shirts, M. R.; Chodera, J. D. *J. Chem. Phys.* **2008**, *129*, 124105.
(11) Tan, Z.; Gallicchio, E.; Lapelosa, M.; Levy, R. M. *J. Chem. Phys.* **2012**, *136*, 144102.
(12) Lee, T.-S.; Radak, B. K.; Pabis, A.; York, D. M. *J. Chem. Theory Comput.* **2013**, *9*, 153−164.
(13) Lee, T.-S.; Radak, B. K.; Huang, M.; Wong, K.-Y.; York, D. M. *J. Chem. Theory Comput.* **2014**, *10*, 24−34.
(14) Laio, A.; Parrinello, M. *Proc. Natl. Acad. Sci. U.S.A.* **2002**, *99*, 12562−12566.
(15) Darve, E.; Pohorille, A. *J. Chem. Phys.* **2001**, *115*, 9169−9183.
(16) Darve, E.; Rodriguez-Gomez, D.; Pohorille, A. *J. Chem. Phys.* **2008**, *128*, 144120.
(17) Maragliano, L.; Vanden-Eijnden, E. *Chem. Phys. Lett.* **2006**, *426*, 168−175.
(18) Rosso, L.; Minary, P.; Zhu, Z.; Tuckerman, M. E. *J. Chem. Phys.* **2002**, *116*, 4389−4402.
(19) Abrams, J. B.; Tuckerman, M. E. *J. Phys. Chem. B* **2008**, *112*, 15742−15757.
(20) Chen, M.; Cuendet, M. A.; Tuckerman, M. E. *J. Chem. Phys.* **2012**, *137*, 024102.
(21) Maragakis, P.; van der Vaart, A.; Karplus, M. *J. Phys. Chem. B* **2009**, *113*, 4664−4673.
(22) Kolmogorov, A. N. *Izv. Akad. Nauk SSSR* **1941**, *5*, 3−14.
(23) Wiener, N. *Extrapolation, Interpolation and Smoothing of Stationary Time Series*; MIT Press: Cambridge MA, 1949.
(24) Matheron, G. *Adv. Appl. Probab.* **1973**, *5*, 439−468.
(25) O'Hagan, A. *J. R. Stat. Soc. B* **1978**, *40*, 1−42.
(26) Williams, C. K. I.; Rasmussen, C. E. In *Advances in Neural Information Processing Systems 8*; Touretzky, D. S., Hasselmo, M. E., Mozer, M. C., Eds.; MIT Press: Cambridge MA, 1996; pp 514−520.
(27) Rasmussen, C. E.; Williams, C. K. I. *Gaussian Processes for Machine Learning (Adaptive Computation and Machine Learning series)*; MIT Press: Cambridge MA, 2005.
(28) Bartók, A. P.; Payne, M. C.; Kondor, R.; Csányi, G. *Phys. Rev. Lett.* **2010**, *104*, 136403.
(29) Bartók, A. P.; Gillan, M. J.; Manby, F. R.; Csányi, G. *Phys. Rev. B* **2013**, *88*, 054104.
(30) Rupp, M.; Tkatchenko, A.; Müller, K.; von Lilienfeld, O. *Phys. Rev. Lett.* **2012**, 058301.
(31) Handley, C. M.; Hawe, G. I.; Kell, D. B.; Popelier, P. L. A. *Phys. Chem. Chem. Phys.* **2009**, *11*, 6365.
(32) Bartels, C.; Karplus, M. *J. Comput. Chem.* **1997**, *18*, 1450−1462.
(33) Bartels, C. *Chem. Phys. Lett.* **2000**, *331*, 446−454.
(34) Zhu, F.; Hummer, G. *J. Comput. Chem.* **2011**, *33*, 453−465.
(35) MacKay, D. J. C. *Information Theory, Inference and Learning Algorithms*, 1st ed.; Cambridge University Press: Cambridge, UK, 2003.
(36) MacKay, D. J. C. *NATO ASI Series F Computer and Systems Sciences* **1998**, *168*, 133−166.

(37) Sokal, A. D. *Monte Carlo Methods in Statistical Mechanics: Foundations and new Algorithms*; Cours de Troisième Cycle de la Physique en Suisse Romande: Lausanne, 1989.
(38) Flyvbjerg, H.; Petersen, H. G. *J. Chem. Phys.* **1989**, *91*, 461−466.
(39) Kobrak, M. N. *J. Comput. Chem.* **2003**, *24*, 1437−1446.
(40) Rasmussen, C. E. *Bayesian Statistics* **2003**, *7*, 651−659.
(41) Sprik, M.; Ciccotti, G. *J. Chem. Phys.* **1998**, *109*, 7737−7744.
(42) Bonomi, M.; Branduardi, D.; Bussi, G.; Camilloni, C.; Provasi, D.; Raiteri, P.; Donadio, D.; Marinelli, F.; Pietrucci, F.; Broglia, R. A.; Parrinello, M. *Comput. Phys. Commun.* **2009**, *180*, 1961−1972.
(43) MacKerell, A.; Bashford, D.; Bellott, M.; Dunbrack, R.; Evanseck, J.; Field, M.; Fischer, S.; Gao, J.; Guo, H.; Ha, S.; Joseph-McCarthy, D.; Kuchnir, L.; Kuczera, K.; Lau, F.; Mattos, C.; Michnick, S.; Ngo, T.; Nguyen, D.; Prodhom, B.; Reiher, W.; Roux, B.; Schlenkrich, M.; Smith, J.; Stote, R.; Straub, J.; Watanabe, M.; Wiorkiewicz-Kuczera, J.; Yin, D.; Karplus, M. *J. Phys. Chem. B* **1998**, *102*, 3586−3616.
(44) Schneider, T.; Stoll, E. *Phys. Rev. B* **1978**, *17*, 1302−1322.
(45) Plimpton, S. *J. Comput. Phys.* **1995**, *117*, 1−19.
(46) Grossfield, A. An implementation of WHAM: the Weighted Histogram Analysis Method. http://membrane.urmc.rochester.edu/content/wham/ (accessed 26 Jan 2012), version 2.0.6.
(47) York Group. http://theory.rutgers.edu/Group/vFep.shtml (accessed 17 Jan 2014), version 0.2.1003_1388675964.

■ NOTE ADDED IN PROOF

After the acceptance of this paper, a paper by M. A. Cuendet and M. E. Tuckerman [J. Chem. Theory Comput., 2014, doi 10.1021/ct500012b] used a non-Bayesian kriging method to combine histogram and gradient information for the reconstruction of free energies, but found no consistent improvement from using both types of data.